Delft University of Technology

Design and power calculation of HLFC suction system for a subsonic short-range aircraft

Prasannakumar, Adarsh; Wolff, Johannes; Radespiel, Rolf; Boermans, Loek; Hühne, Christian; Badrya, Camli

DOI
10.1007/s13272-022-00614-1

Publication date
2022

Document Version
Final published version

Published in
CEAS Aeronautical Journal

Citation (APA)
Prasannakumar, A., Wolff, J., Radespiel, R., Boermans, L., Hühne, C., & Badrya, C. (2022). Design and power calculation of HLFC suction system for a subsonic short-range aircraft. *CEAS Aeronautical Journal*, *13*(4), 1003-1026. https://doi.org/10.1007/s13272-022-00614-1

Important note
To cite this publication, please use the final published version (if applicable).
Please check the document version above.

Copyright
Other than for strictly personal use, it is not permitted to download, forward or distribute the text or part of it, without the consent of the author(s) and/or copyright holder(s), unless the work is under an open content license such as Creative Commons.

Takedown policy
Please contact us and provide details if you believe this document breaches copyrights.
We will remove access to the work immediately and investigate your claim.

This work is downloaded from Delft University of Technology.
For technical reasons the number of authors shown on this cover page is limited to a maximum of 10.

CEAS Aeronautical Journal
https://doi.org/10.1007/s13272-022-00614-1

ORIGINAL PAPER

Design and power calculation of HLFC suction system for a subsonic short-range aircraft

Adarsh Prasannakumar[1] · Johannes Wolff[2] · Rolf Radespiel[1] · Loek Boermans[3] · Christian Hühne[2] · Camli Badrya[1]

Received: 31 March 2021 / Revised: 26 August 2022 / Accepted: 31 August 2022
© The Author(s) 2022

Abstract

Hybrid laminar flow control (HLFC) can be a possible solution for future sustainable energy-efficient aviation. The current study proposes a MATLAB-based numerical tool for the design of the suction system for an airfoil optimized for a subsonic short-range HLFC application. Considerable energy losses may occur when the air passes through the perforated metallic outer surface and the inner structure of the suction system. A semi-empirical approach is used to design a layout that provides a target suction velocity based on measured pressure losses through porous medium and substructures. Flowbench measurements were performed on 3D-printed internal core test samples to quantify the pressure losses that can be used to create a lower pressure below the porous sheet matching the target suction velocity. The actual suction realized on the airfoil using this substructure concept has a discrete nature that increases with the distance between two adjacent walls. Finally, the suction system's power requirement is calculated. The power requirement for distributed suction accounts for the pressure loss characteristics of the porous material, the internal core structure, and throttling holes. However, the study does not include the ducting losses from the substructure to the compressor. Approximately 80% of the total suction power is utilized to eject the sucked air back to the freestream conditions for a system with a compressor and propulsive system efficiency equal to one. The study analyses the performance of the designed internal core layout to different flight conditions and addresses the suction power requirement variation with lift coefficient and flight altitude.

Keywords xHLFC · HLFC · Laminar flow control · Boundary layer suction · Suction system · Suction power · Internal structure

List of symbols

p_∞	Atmospheric pressure (Pa)
p_o	Total pressure at freestream conditions (Pa)
p_e	Static pressure on airfoil (Pa)
$p_{pump,in}$	Pressure at inlet side of suction pump (Pa)
U_∞	Flight velocity (ms^{-1})
U_e	Boundary layer edge velocity (ms^{-1})
ρ_0	Density of air at mean sea level (kgm^{-3})
ρ	Density of air at flight altitude (kgm^{-3})
μ_0	Dynamic viscosity of air at mean sea level ($kgm^{-1}s^{-1}$)
μ	Dynamic viscosity of air at flight altitude ($kgm^{-1}s^{-1}$)
d	Hole diameter (m)
ds	Small portion of suction region considered (m)
t	Thickness (m)
Q	Volume flow rate (m^3s^{-1})
c	Chord of airfoil (m)
v	Target local suction velocity (ms^{-1})
V_s	Actual velocity (ms^{-1})
$\overline{h}$	Average height of the suction stream tube (m)
$\overline{u}$	Velocity at $\overline{h}$ (ms^{-1})
Q_s	Total suction volume flow rate through the porous sheet (m^3s^{-1})
w_{ps}	Distance between center to center of adjacent holes (Hole pitch) (m)
$l_{ps_{entry}}$	Entry length for flow to become fully developed (m)

✉ Adarsh Prasannakumar
a.prasannakumar@tu-braunschweig.de

Camli Badrya
c.badrya@tu-bs.de

1 Institute of Fluid Mechanics, Cluster of Excellence SEA- Sustainable and Energy-Efficient Aviation, TU Braunschweig, Braunschweig, Germany

2 Institute of Mechanics and Adaptronics (IMA), Cluster of Excellence SEA-Sustainable and Energy-Efficient Aviation, TU Braunschweig, Braunschweig, Germany

3 Delft University of Technology, Delft, The Netherlands

Published online: 14 September 2022

t_{ps}	Thickness of the porous sheet (m)
Δp	Pressure drop (Pa)
V_h	Velocity inside the porous sheet hole (ms^{-1})
M_h	Mach number inside the porous sheet hole
a,b	Bohning–Doerffer model coefficients
B	Wall shear stress coefficient $\left(\frac{\tau_w}{\frac{\rho_h V_h^2}{2}}\right)$
P'	Power per unit span (Wm^{-1})
P	Power (W)
C_p	Pressure coefficient
C_q	Local suction coefficient $\left(\frac{v}{U_\infty}\right)$
C_Q	Integrated suction coefficient $\left(\int \frac{v}{U_\infty} d\left(\frac{s}{c}\right)\right)$
C_f	Local skin friction coefficient
$C_{d_{s,ideal}}$	Minimum suction drag coefficient
C_{d_s}	Suction drag coefficient
C_l	Lift coefficient of the airfoil
χ	Velocity profile parameter $\left(\frac{u}{u_{mean}} - 1\right)$
Re	Reynolds number $\left(\frac{V_d}{\nu}\right)$
Re_k	Reynolds number of suction streamtube $\left(\frac{\overline{hu}}{\nu}\right)$
P60	Porous sheet of perforation 60 µm
P120	Porous sheet of perforation 120 µm
P240	Porous sheet of perforation 240 µm

Subscript

ps	Porous sheet
ic	Internal core
thr	Throttling hole

1 Introduction

For sustainable aviation, it is vital to carry out detailed research for developing different drag reduction technologies for aircraft. The current study deals with one such technology called Laminar Flow Control (LFC), which focuses on the viscous drag reduction employing boundary layer suction. The major component of drag in airfoil is viscous drag which contributes to half of the total aircraft drag [1]. The skin friction coefficient of turbulent flow is significantly higher than that for laminar flow, therefore aircraft manufacturers employ flow control to delay the laminar-turbulent transition. Natural Laminar Flow (NLF) airfoil is one such passive flow control method, where the shaping of the airfoil controls the transition location [2]. This passive laminar flow control method is effective for low flight speeds up to a Mach number of 0.75 and up to a leading edge sweep of 23° [1]. Due to the limitation of passive flow control at higher flight velocities, active laminar flow control was developed, which can delay transition further by using boundary layer suction. LFC sucks small portions of air from the boundary layer with the help of a perforated skin on the airfoil. The structural constraints limit the practical application of employing suction throughout the airfoil chord due to the wing box and add additional weight penalty due to complex suction systems [3]. Due to these reasons, the possibility of combining the advantages of NLF and LFC was adapted, which is termed as Hybrid Laminar Flow Control—HLFC [3]. Most of the previous work in HLFC employed boundary layer suction close to leading-edge followed by natural laminar flow airfoil with a potential drag reduction of 15% [4].

Previous HLFC system developed by DLR (Deutsches Zentrum für Luft-und Raumfahrt, German Aerospace Research Center), achieved the suction profile either through individual chamber control in the suction region or simplified ALTTA concept where the throttle holes are used to control the suction velocity using a single plenum [5]. DLR also developed a more advanced technology called Tailored Skin Single Duct (TSSD) [6] which uses a multilayered tailored outer skin. TSSD concept eliminates internal chambers by carefully designing the permeability of the external porous sheet. Both the ALTTA and TSSD concepts applied boundary layer suction on the leading edge surface. The transition due to cross-flow instabilities (CFI) is avoided using suction near the leading edge, thereby making sure the transition is predominated by Tollmien–Schlichting instabilities (TSI) after that. The growth of TSI is controlled by shaping the airfoil to create an accelerating flow on the airfoil, thereby ensuring a favorable pressure gradient to dampen the TSI instabilities.

To further extend the drag reduction capability of the HLFC system, Cluster of Excellence of Sustainable and Energy Efficient Aviation (SE2A) investigates the feasibility of extending the natural laminar flow to maintain minimum 80% laminarisation on the airfoil. To achieve this, natural laminar flow is extended further downstream as possible by shaping the airfoil and then employing boundary layer suction to maintain to at least 80% of the chord. On the airfoil, the suction velocity profile trend should resemble the static pressure variation on the outer surface of the airfoil to minimise the power requirement. This concept is termed as xHLFC (extended HLFC) and requires combined optimization of the airfoil shape, suction velocity profile and the internal suction system architecture. The present study considers a previously optimized xHLFC airfoil for a subsonic short-range aircraft [7] as a case study and focuses on the internal suction system design. The airfoil under consideration has been optimized for natural laminar flow till 50% and has a boundary layer suction region which extends from 50 to 80% of the chord. The study proposes a design approach for obtaining the target suction profile by designing the internal layout of the suction system. Figure 1 shows the

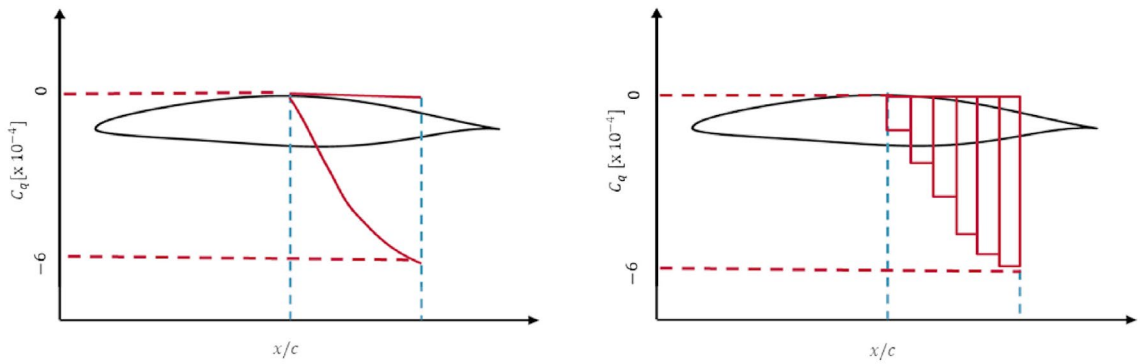

(a) Target suction profile (Adapted from [7])

(b) Actual suction profile on airfoil

Fig. 1 Discrete nature of the actual suction profile compared to target suction profile

difference between target suction profile and actual suction profile achieved on the airfoil.

The suction system includes a suction pump that sucks the air from the boundary layer through a micro-perforated porous metallic sheet supported on an internal core structure. The internal core has two main functions: (1) to provide the variation of the internal pressure to achieve the designed suction velocity along the chord, and (2) to support the porous sheet. Suction system design should consider both aerodynamic and structural constraints [8], but the current study only deals with the aerodynamic requirement of achieving the target suction velocity, characterizing the pressure losses through the suction system and calculating the required suction power. The target suction profile assumes a continuous suction throughout the suction region, but the use of porous sheet and the substructure convert it into a discrete suction. The design approach should include these system-level dependencies to make sure the actual suction profile closely follows the target suction needed for the airfoil.

For calculating the actual suction, the study developed a MATLAB-based code called Actual Suction Power Calculation Tool-ASPeCT to derive the optimum layout of the substructure and calculate the power to suck the required air and accounts for the energy losses in porous medium and the substructure. The substructure is combined with an internal core structure and throttle holes. Figure 2 shows the simple substructure with straight stringer internal core. The space between two stringers including the porous sheet is referred to as a cell in the paper. The internal core structure creates an additional pressure loss inside and along the chord in contrast to the ALTTA (DLR) concept which had individual throttle holes in each cell. This additional control of pressure through the substructure allows to achieve a suction profile that resembles the target suction with minimum pressure losses.

There are three main objectives for the present study. The first part of the study deals with the characterization of the perforated metallic outer sheet used in the suction

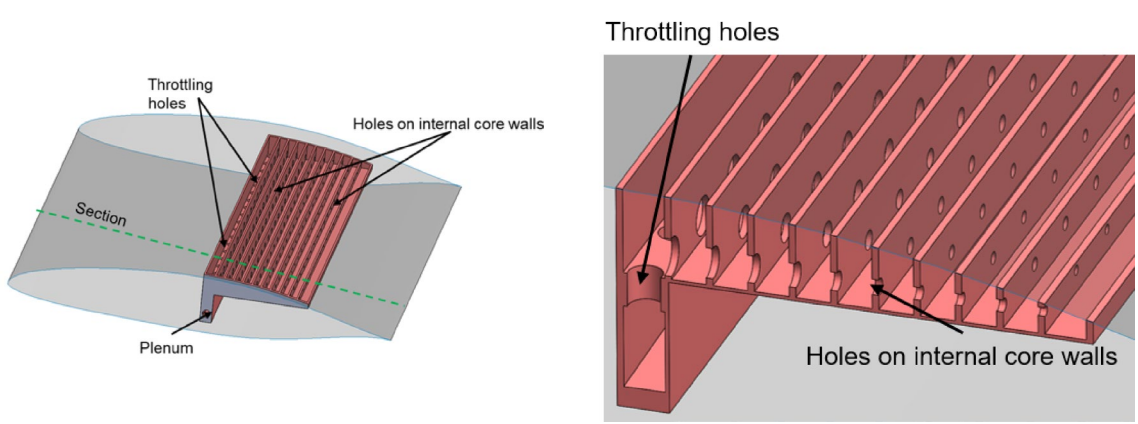

(a) 3D model of the suction system for unswept wing

(b) Suction system sectional view

Fig. 2 Three-dimensional schematic of the substructure of the xHLFC suction system

system. The study investigates the pressure characteristics of the porous sheet manufactured using micro-laser drilling process. The diameter of the perforation and the hole pitch decides the porosity of the metal sheet. The present work considers three micro-perforated samples of perforation diameter 60 µm, 120 µm and 240 µm. Previous measurements of the perforated sheet in wind tunnel helped in modifying the Bohning–Doerffer semi-empirical model [9] to account for the aerodynamic porosity of the porous samples [10]. The revised model also accounts for the increased pressure drop due to suction from the tangential flow on top of the airfoil as a function of Mach number and wall shear stress.

The suction through perforated sheets generates a streamtube over the perforation surface. This streamtube introduces small vortices to the flow as shown in Fig. 3, which can induce transition. For an isolated perforation, the size of the streamtube depends on the velocity profile, the size of the perforation and the flow rate through it. Therefore care should be taken during the selection of these parameters to ensure that the transition is not triggered on the HLFC surface for the required suction requirements.

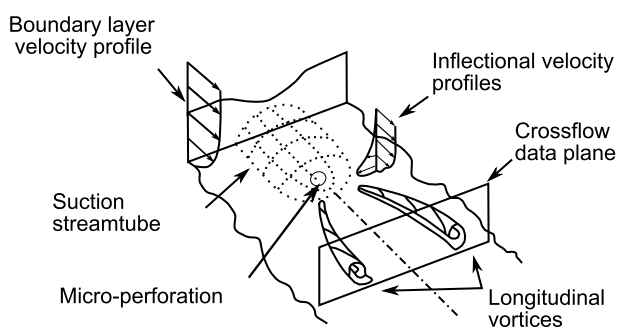

Fig. 3 Schematic of flowfield induced by suction through micro-perforation (adapted from [11])

The second part of the study quantifies the pressure drop characteristics of the internal core structure. The internal core structure is a critical part of the system which defines the actual suction profile through a controllable pressure drop below the porous sheet. Holes of different diameter are provided on the walls of the internal core to create the static pressure variation underneath the porous sheet to enable suction. Numerous samples need to be tested to study the hole diameter's sensitivity to the pressure drop. The pressure distribution of the internal core is determined as a function of the hole diameter based on flowbench measurements and then compared with the analytical values predicted by Goldstein theory of pressure loss through a single hole [12].

The final part deals with the power calculation for the suction system. As an initial step, continuous suction referred to as "target suction velocity profile" is considered over the airfoil and the suction power required to obtain this target suction is calculated. However, in reality the suction pump should also account for the additional power to overcome the energy losses in the porous sheet, internal core and throttle holes as well as any reduction in the suction surface due to gluing or blockages. The present study aims to quantify the power to enable boundary layer suction by overcoming the pressure losses through the porous sheet, the internal structure and the throttle holes.

2 Methodology

Figure 4 shows the design schematic of an xHLFC suction system. For simplicity, the figure shows only a single buffer. A collection of cells along the chordwise direction is termed as a buffer. At the end of each buffer, a throttle hole at the

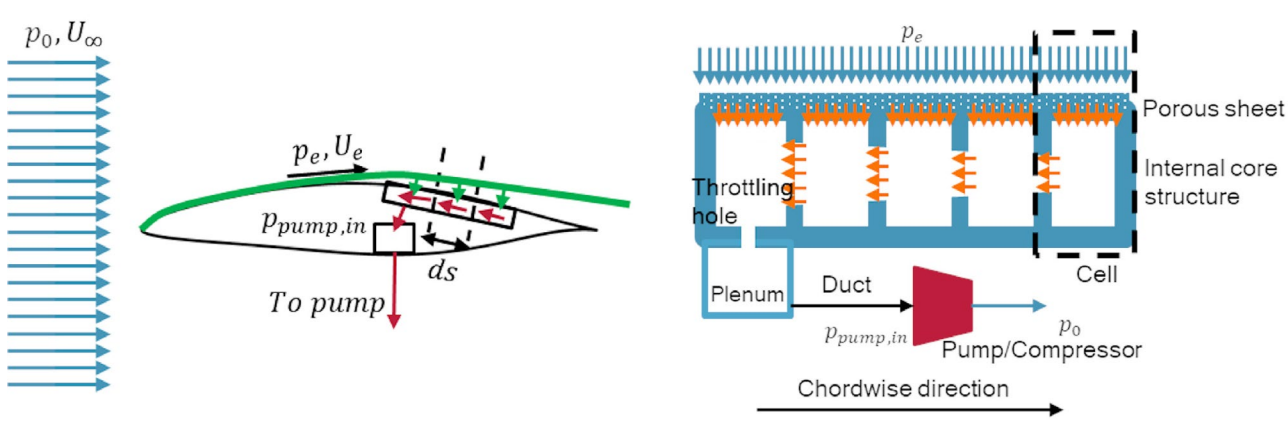

(a) Airflow path in xHLFC suction system

(b) Flow in the internal structure of xHLFC suction system

Fig. 4 Schematic of xHLFC suction system

base of the internal core connects to a plenum chamber where air pressure is stabilized to ensure uniform suction along the spanwise direction. Suction pump or compressor will be connected to the plenum using an internal duct.

Figure 4a shows an airfoil at a flight velocity of U_∞ with boundary layer suction applied at the rear side. The static pressure p_e and velocity U_e are the values at the edge of the boundary layer formed on the airfoil. The green arrows represents the air from the boundary layer moving into the suction system through the porous sheet. The outer pressure increases on the airfoil surface between 50 and 80% chord (adverse pressure region). Red arrows in Fig. 4a represent the air moving through walls of the internal core and finally entering the plenum chamber. Air enters the plenum chamber through throttle holes provided at the bottom surface of the final cell. Although small amounts of air is sucked, considerable energy losses occur as it moves through the porous sheet and the internal core which determines the plenum pressure $p_{\text{pump,in}}$.

Depending on the flight conditions, the shape of the airfoil as well as the maximum diameter of the hole possible in the internal core, the number of buffers may vary to match the target suction velocity. The multi-buffer design can provide more control in terms of area of active suction, which might be useful for certain off-design conditions of the aircraft but adds complexity for the need of separate plenums. The code developed for calculating the optimum layout of the internal core is explained in Sect. 2.1.

2.1 ASPeCT

Actual Suction Power Calculation Tool (ASPeCT) is a MATLAB-based code developed to calculate the optimum layout for the internal core and the corresponding suction power. ASPeCT follows a similar approach used to optimize the suction system for sailplanes [13]. While the method in reference [13] was used to optimize a specific internal structure arrangement (triangular folded core concept), ASPeCT can handle various concepts of internal structures due to the module-based architecture. The program uses separate modules to manage the properties and pressure loss characteristics of the xHLFC system components. Figure 5 shows the architecture of the code.

The code requires boundary layer edge velocity and skin friction coefficient over the airfoil along with the suction velocity coefficient as inputs. For this, the present study performs numerical calculations using XFOILSUC [14–17] for the range of lift coefficients. The program calculates the optimum chamber, which includes the number of cells, the hole diameter required in cell walls and the throttle hole diameter needed to produce the required suction velocity through the porous sheet. At first, the code converts the local suction coefficient (non-dimensional) to velocity (dimensional) by

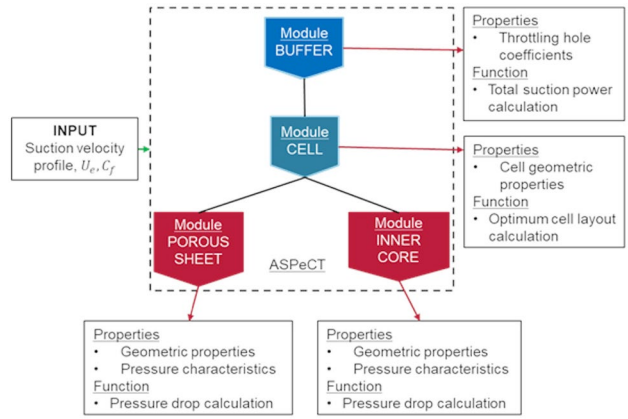

Fig. 5 Flowchart of ASPeCT

multiplying with the flight velocity. The averaged suction velocity through the open area of the suction surface is then calculated to determine the volume flow in each cell. Using the volume flow rate and the local outer pressure above the neighbouring cell (in the direction of leading edge), the hole diameter between the two cell is estimated. Figure 6 shows the optimization routine for the buffer used in the code.

The lowest static pressure will be in the cell closest to the leading edge. Through the throttle holes at the bottom surface of this cell, air moves into the plenum chamber. The plenum chamber pressure can be estimated based on the lowest static pressure inside the cell closest to the leading edge and the pressure loss through the throttle hole. The present study assumes the plenum chamber pressure as the inlet pressure of the suction pump (neglecting duct losses from plenum to compressor). Suited suction velocity may not be obtained for certain locations on the porous sheet cases due to structural (maximum hole diameter possible) and geometrical limitations of the internal core. In these cases, multi-buffer approach can be used. Finally, ASPeCT delivers three outputs (1) The actual suction velocity, (2) The internal core layout, and (3) The suction power and volume flow requirement at different lift coefficients. Section 2.2 shows the power calculation for the suction system.

2.2 Power estimation

This section presents the power calculation for the suction system, and the main aim is to understand how the xHLFC suction system design affects the required power. The paper presents the derivation of power in a step-by-step procedure. As a first step, the power calculation for an airfoil, as shown in Fig. 4a. The power required by the compressor can be calculated thermodynamically by assuming a reversible adiabatic flow as explained in references [18, 19]. However, for this detailed calculation, the temperature at the inlet side of the compressor is required.

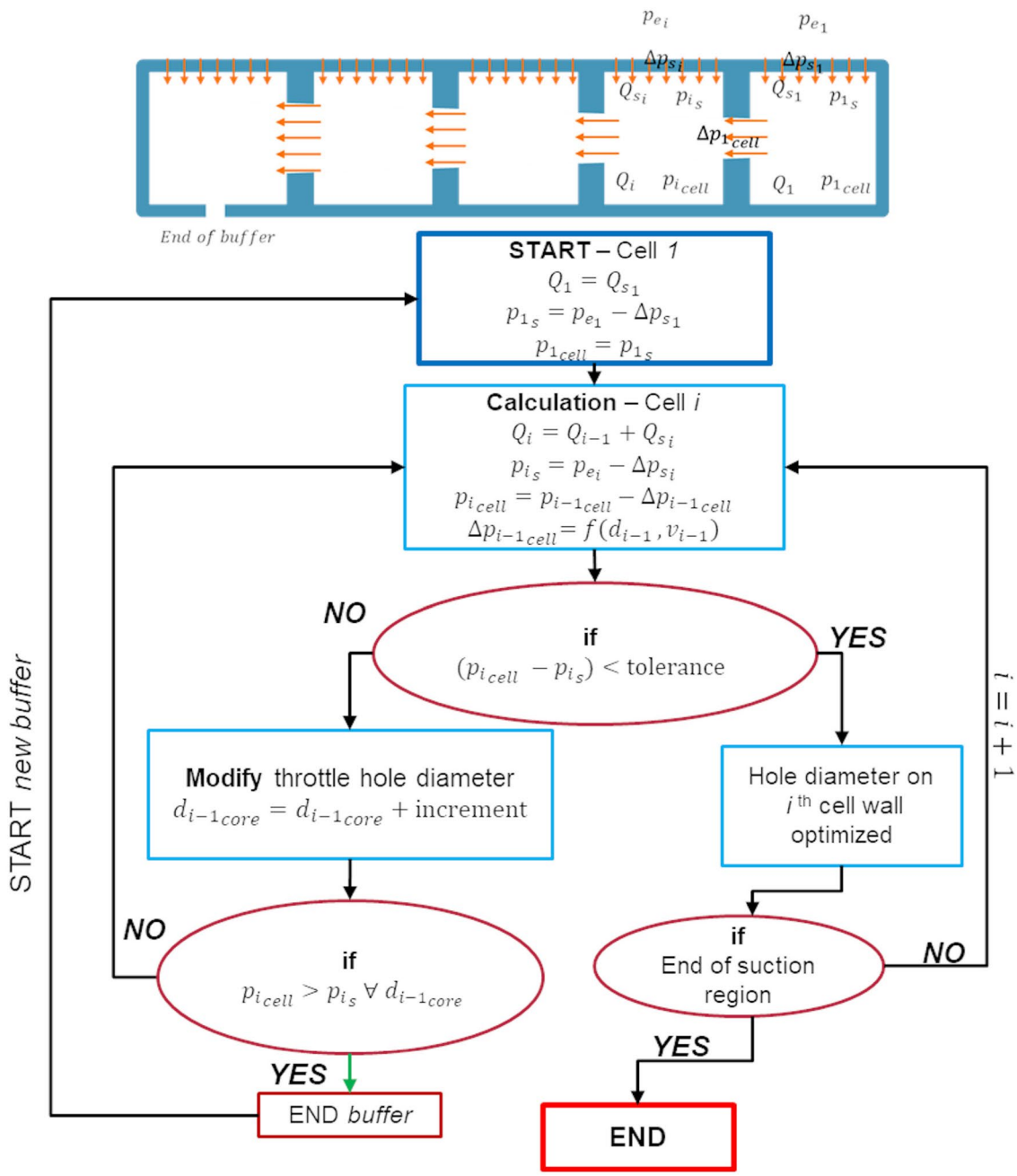

Fig. 6 Flowchart of ASPeCT code

Since the temperature change of air as it passes through the perforated sheet and internal structure is not taken into account, this cannot be accurately estimated. Therefore as a preliminary approach, a power calculation method based on reference [20] is adopted. The power required for suction per unit span is estimated based on the working pressure difference of the compressor and the volume flow rate.

The suction pump used in the suction system is assumed to increase the pressure of the sucked air ($p_{\text{pump,in}}$) back to the freestream total pressure. Equation 1 gives area the pump power per span for the suction region shown in Fig. 4a.

$$P'_{\text{pump}} = \frac{1}{\eta_{\text{p}}} \int \left(p_0 - p_{\text{pump,in}}\right) v \mathrm{d}s \tag{1}$$

η_p is the efficiency of the suction pump and p_0 is the freestream total pressure. If we consider the suction pump to be driven by the propulsive system of the aircraft with efficiency η_a, the suction pump power can also be calculated in terms of an equivalent drag coefficient, as shown in Eq. 2. This drag coefficient is defined as suction drag coefficient C_{d_s} [20]. The suction drag coefficient can be written as shown in Eq. 3.

$$P'_{\text{pump}} = \frac{\left(C_{d_s}\frac{1}{2}\rho U_\infty^2\right)cU_\infty}{\eta_a} \tag{2}$$

$$C_{d_s} = \frac{\eta_a P'_{\text{pump}}}{\frac{1}{2}\rho U_\infty^2 cU_\infty} \tag{3}$$

For the current study, the suction pump's efficiency and the efficiency of the propulsive system are treated as unity ($\eta_a = \eta_p = 1$). With this assumption and substituting Eq. 1 in Eq. 3, the suction drag coefficient can be re-formulated as:

$$C_{d_s} = \int \frac{\left(p_0 - p_{\text{pump,in}}\right)}{\frac{1}{2}\rho U_\infty^2}\frac{v}{U_\infty}d\left(\frac{s}{c}\right) \tag{4}$$

$$C_{d_s} = \int \left[\frac{\left(p_0 - p_e\right)}{\frac{1}{2}\rho U_\infty^2} + \frac{\left(p_e - p_{\text{pump,in}}\right)}{\frac{1}{2}\rho U_\infty^2}\right]\frac{v}{U_\infty}d\left(\frac{s}{c}\right) \tag{5}$$

2.2.1 Ideal pump power

For suction employed on a thin boundary layer on the airfoil, the pressure gradient normal to the chord in the boundary layer is negligible [21]. Therefore, the pressure at the edge of the boundary layer, p_e, is assumed as the pressure on the outer surface of the suction panel. The ideal pump power is estimated assuming negligible pressure losses in the suction system. The plenum pressure is calculated from minimum static pressure value on the suction region of the airfoil. The difference between static pressure outside the suction panel (p_e) and the pump pressure ($p_{\text{pump}_{\text{in}}}$) is relatively small compared to the difference between p_e and the total pressure of the freestream (p_0). The major component of the power is termed as ideal power of the suction system. Equation 6 shows the Bernoulli relation applied in the inviscid region between freestream and edge of the boundary layer where the velocity is U_e

$$p_0 = p_e + \frac{1}{2}\rho U_e^2 = p_\infty + \frac{1}{2}\rho U_\infty^2 \tag{6}$$

For the small suction segment ds considered here , the static pressure p_e can be treated as a constant for that segment and the total suction will be the summation of these small segments over the suction region. Equations 5 and 6 can be combined to derive the Ideal suction drag coefficient, as presented in Eq. 7.

$$\begin{aligned} C_{d_{\text{s,ideal}}} &= \int \left(-C_p + 1\right)\frac{v}{U_\infty}d\left(\frac{s}{c}\right) \\ &= \int \left(\frac{U_e}{U_\infty}\right)^2\frac{v}{U_\infty}d\left(\frac{s}{c}\right) \end{aligned} \tag{7}$$

The suction drag coefficient can be converted to power using Eq. 3 by multiplying the free stream dynamic pressure and the suction volume flow rate as given by Equation 8.

$$P'_{\text{ideal}} = C_{d_{\text{s,min}}}\frac{1}{2}\rho {U_\infty}^2 cU_\infty \tag{8}$$

2.2.2 Actual power

The actual suction power includes the ideal power as well as the minor component corresponding to the pressure loss $p_e - p_{\text{pump,in}}$. This additional power is needed to compensate the energy losses through the three main components of the suction system namely the porous sheet, internal core and the throttle hole. Equation 9 shows the actual power calculation for the boundary layer suction system.

$$\begin{aligned} P'_{\text{pump}} = \frac{1}{\eta_p}\Bigg[&\left[\left(p_\infty - p_{\text{pump,in}}\right) + \frac{1}{2}\rho U_\infty^2\right] \\ &\cdot \int v\text{d}s + \Delta p_{\text{ps}} \cdot \int v\text{d}s \\ &+ \Sigma\Delta p_{\text{ic}} \cdot \frac{Q_{\text{ic}}}{\text{span}} + \Delta p_{\text{thr}} \cdot \int v\text{d}s\Bigg] \end{aligned} \tag{9}$$

$$P'_{\text{pump}} = P'_{\text{ideal}} + P'_{\text{ps}} + P'_{\text{ic}} + P'_{\text{thr}} \tag{10}$$

The additional component of power that includes P'_{ps}, P'_{ic} and P'_{thr} is termed as buffer power. The buffer power depends on the pressure characteristics of the suction system. Therefore in order to calculate the total power requirement of the suction system, the pressure characteristics of the porous sheet, the internal core structure and throttle holes need to be estimated. These pressure coefficients are determined empirically as described in Sect. 3 and compared with the analytical model explained in Sects. 2.3 and 2.4.

2.3 Pressure loss through the perforated sheet

The analytical model for the porous metallic sheet is selected based on the following assumptions.

1. Pressure drop for air through suction from stagnant air is considered based on the experimental measurements. The additional pressure loss due to the tangential flow and formation of the boundary layer is modeled based on the semi-empirical model based on previous work [10].
2. The study neglects the effect of neighboring holes on pressure loss. It is reasonable as all the samples under investigation have an inter-hole distance of ten times the hole diameter. Previous studies showed that the effect of the hole wake is minimum for a pitch of ten times the diameter of the holes [11].

In the present study, a semi-empirical approach is followed to calculate the porosity coefficients in a similar manner to two-coefficient equation proposed by Priest [22]. Equation 11 shows the pressure drop through the porous sheet as a function of velocity through it.

$$\Delta p_{\mathrm{ps}} = C_{\mathrm{ps},2} V_{\mathrm{ps}}^2 + C_{\mathrm{ps},1} V_{\mathrm{ps}} \tag{11}$$

$C_{\mathrm{ps},1}$ and $C_{\mathrm{ps},2}$ are defined as the porosity coefficients of the porous sheet. Based on this model, it is expected that the pressure loss through porous sheets varies as a quadratic function of velocity. The coefficient $C_{\mathrm{ps},2}$ is scaled with density and the coefficient $C_{\mathrm{ps},1}$ is scaled with dynamic viscosity. Therefore, for the porosity coefficients can be scaled to different atmospheric conditions as shown in Eq. 12 [22].

$$\Delta p_{\mathrm{ps}} = C_{\mathrm{ps},2} \frac{\rho}{\rho_0} V_{\mathrm{ps}}^2 + C_{\mathrm{ps},1} \frac{\mu}{\mu_0} V_{\mathrm{ps}} \tag{12}$$

The porosity parameters calculated from the curve-fit of the measured data are used in ASPeCT to calculate the suction power through porous medium. The calculated porosity coefficients will reflect the actual pressure characteristics of the perforation taking into account the irregularities of the manufacturing process. Measurements make it possible to fine-tune the analytical model's coefficients further to compensate for these non-ideal effects.

Apart from this, an additional pressure drop is expected when the suction occurs from a tangential stream above the airfoil. This is due to the blocking effect caused by inertia of the incoming flow [9] (Fig. 7).

Bohning and Doerffer showed that the tangential flow creates a blocking effect for suction through the perforated sheet [9] and increases the pressure losses through it when compared to suction from still air. This blocking effect was related to the shear stress exerted by the tangential air stream at the surface of the perforated sheet. The pressure drop was accounted and compared to the semi-empirical Bohning–Doerffer (B–D) model and modifications to the model were proposed [10]. The modified empirical model shown in Eq. 13 will be used in the current study.

$$\frac{\Delta p_{\mathrm{ps}_{\mathrm{tan}}}}{p_0} = M_{\mathrm{h}}^{\frac{1}{0.5}} b \left(B M_{\mathrm{h}}^{\frac{1}{a}} \right) \tag{13}$$

M_{h} is the Mach number inside the hole, $B = \frac{\tau_w}{\frac{\rho_{\mathrm{h}} V_{\mathrm{h}}^2}{2}}$ is the wall shear stress coefficient. The coefficients a and b are properties of the porous sheet calculated empirically. Once the pressure drop through the porous sheet is known, the corresponding power can be calculated using Eq. 14.

$$P_{\mathrm{ps,cell}} = Q_{\mathrm{cell}} \Delta p_{\mathrm{ps,cell}} \tag{14}$$

Q_{cell} and $\Delta p_{\mathrm{ps,cell}}$ are the volume flow rate through the porous sheet and the pressure drop inside a cell, respectively.

2.4 Pressure loss through internal core structure

Pressure loss experienced by the air as it moves through the holes provided in the internal core walls is modelled using Goldstein analytical model for a circular pipes [12]. Stringer wall thickness in the measured samples is kept constant at 0.8 mm, and hole diameter is varied between 2 and 6 mm with 1 mm increment for the measurement. Goldstein studied the effect of velocity profile on pressure loss through small pipes and proposed an entry length based on the diameter of

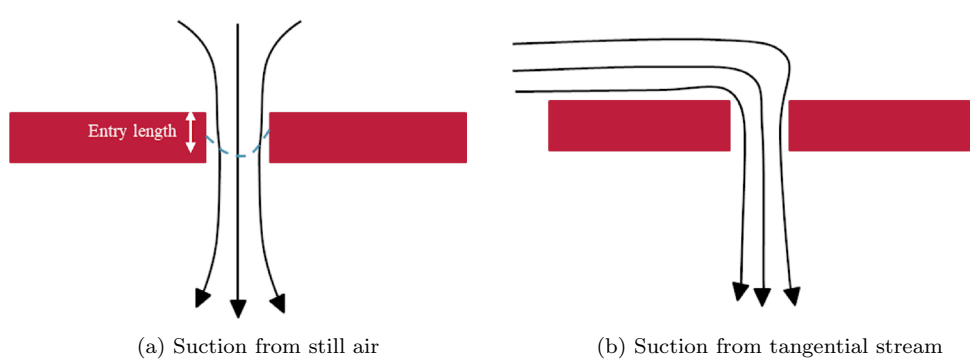

Fig. 7 Illustration of streamlines for suction from still air and tangential flowing air

the pipe and the corresponding Reynolds number (Re). Equation 15 shows the entry length calculated by Goldstein and Eq. 16 shows the analytical model to calculate pressure drop for this case.

$$l_{\mathrm{ps_{entry}}} = 0.06\frac{d_{\mathrm{ps}}}{2}\mathrm{Re_{ps}} \tag{15}$$

$$\Delta p_{\mathrm{ic}} = \left(2\chi + \chi^2\right)\frac{1}{2}\rho V_{\mathrm{ic}}^2 \tag{16}$$

Δp_{ic} is the pressure drop through hole provided in the internal core wall for a velocity V_{ic}. The parameter χ is a function of the velocity profile of the flow inside the hole. χ is estimated from the calculation of Goldstein (Fig. 78, Page 302, [12]) using the thickness of the wall, the hole diameter, and the Reynolds number based on the hole diameter as a function of χ. The power to suck the air through the internal core can also be calculated similarly to that of the porous sheet. Equation 17 is used for this purpose.

$$P_{\mathrm{ic,cell}} = Q_{\mathrm{cell}}\Delta p_{\mathrm{ic,cell}} \tag{17}$$

3 Experimental setup and measurements

To measure the pressure characteristics of the perforated sheet and the internal core, two experimental apparatuses were used in this study: (1) DLR Large flow meter to measure the porosity coefficients of the perforated sheet and (2) Internal core flowbench to measure the internal core samples. This section introduces the experimental set-up and the estimation of the pressure characteristics of the micro-perforated sheets and the inner structure.

3.1 Large flow meter experimental setup

The pressure drop through the porous sheet samples was investigated using DLR large flow meter experimental setup [23]. For pressure measurement the experimental setup uses a 0–15 psi range Paroscientific Digiquartz Model 745 pressure standard. The instrument has 0.008% full scale accuracy. A PT100 temperature sensor with TLOG4 micro-controller with a +/− 0.5 K accuracy is used for measuring the temperature. Based on 95% confidence interval, the mass flow meter has a measurement error of 0.12% caliberated with standard from Physikalisch Technische Bundesanstalt (PTB).

The perforated sheets tested has hole spacing of the test samples are fixed at ten times the hole diameter in a triangular arrangement. Figure 8 shows the pattern of holes on the perforated samples. The porosity is the ratio of the open area to the area of the equilateral triangle formed by connecting the centre of the circles. Equation 18 shows the calculation of porosity of the perforated sheet. Figure 9 shows the three micro-laser drilled metallic samples used for the current study.

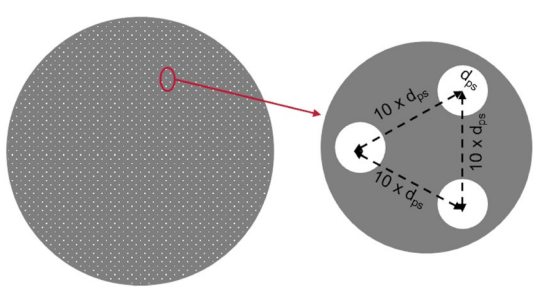

Fig. 8 Perforation pattern on a porous sheet

Table 1 Test samples for micro-drilled porous metallic sheet

Notation	Hole diameter (μm)
P60	60
P120	120
P240	240

Fig. 9 Micro-laser drilled perforated samples

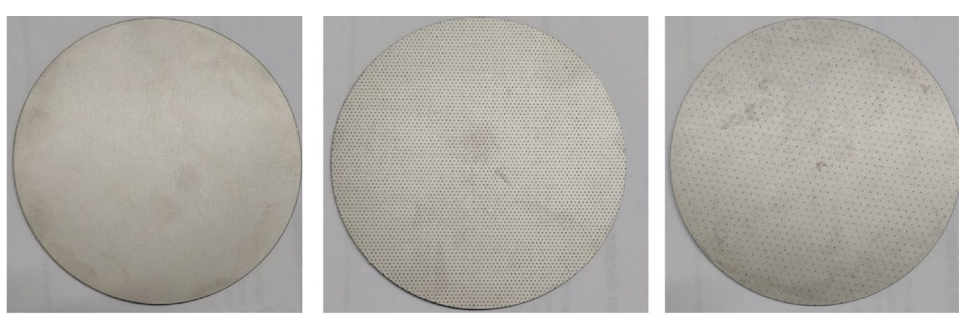

(a) $d_{ps} = 60\ \mu m$ (b) $d_{ps} = 120\ \mu m$ (c) $d_{ps} = 240\ \mu m$

$$\text{Porosity} = \frac{3\left(\frac{1}{6}\right)\pi\left(\frac{d_{ps}^2}{4}\right)}{\frac{\sqrt{3}}{4}\left(10d_{ps}\right)^2} = 0.9\% \tag{18}$$

The power required to suck the air through the porous sheet is then calculated as the product of the pressure loss and the volume flow rate as shown in Eq. 14. Table 1 shows the notations that will be followed for the perforated samples.

3.1.1 Pressure characteristics of micro-perforated sheet

Figure 10 shows the pressure drop through the micro-perforated porous samples P60, P120, and P240. The pressure drop is plotted as a function of velocity inside the hole (based on the open area).

As expected, the pressure drop for a given velocity is larger for the smaller holes. To account for the actual pressure characteristics for the power calculation in ASPeCT, the pressure drop coefficients estimated based on the measured data and corresponding curve fit are used. The Priest pressure model coefficients of the measured porous sheets are calculated using a quadratic curve fit. Second thing to consider is the conditions at which the pressure drop coefficients are estimated. Since the experiments were performed at mean sea level conditions, the coefficients need to be scaled to the flight altitude conditions. This is achieved by modifying the coefficients corresponding to density and viscosity accordingly as explained in Sect. 2.3. Table 2 shows the measured coefficients and those scaled to the flight conditions at 8000 m.

3.2 Internal core flowbench

For measuring the static pressure variation inside the internal core samples, flowbench experimental investigations are carried out on the 3D-printed test specimens. The printed adapter funnel is connected to the suction side that modifies the rectangular cross section of the sample smoothly to a circular cross section of inner diameter of 50 mm. Höntzsch Ta Di 27.2 GE60 volume flow meter with a measuring range of 7–2092 lpm (litres/minute) and measurement inaccuracy of 2% is connected to the funnel to measure the flow rate. Figure 11 shows the test specimen connected to the experiment setup.

As shown in Fig. 11 static pressure is measured at 3 locations along the flow direction. At each of these three locations, 3 pressure taps are fixed to measure the pressure variation normal to the flow direction. A side channel pump from the manufacturer Elektror (0.18 kW) is used to suck the air through the test sample from right to left in Fig. 11.

The flow rate is adjusted based on the velocity through each hole and vary from 1 to 30 m/s. The velocity range is similar to the order of magnitude of velocities for xHLFC application in actual flight. In this setup, the pressure measurement is carried out using Digital Temperature Compensation (DTC) Initium system which has a full-scale accuracy of +/− 0.5%. The measurements have a standard deviation of 1% from mean calculated using a *t* student distribution with a two-sided confidence interval of 95% for 2500 samples at

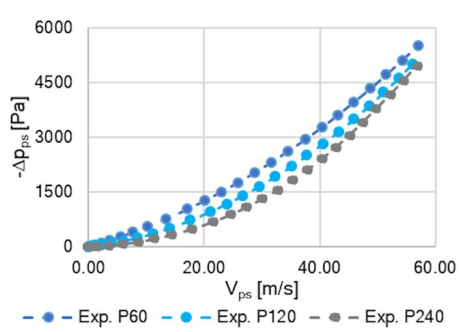

Fig. 10 Internal core structure test sample in flowbench

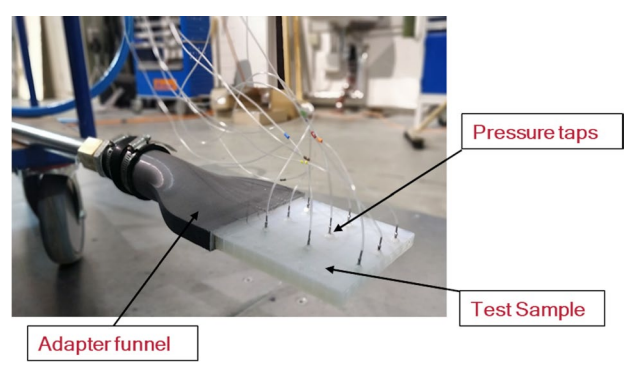

Fig. 11 Internal core structure test sample in flowbench

Table 2 Porosity coefficients of the perforated samples

Sample	Analytical		Experiment		Scaled (experiment)	
	$C_{ps,2,ana.}$	$C_{ps,1,ana.}$	$C_{ps,2}$	$C_{ps,1}$	$C_{ps,2}\frac{\rho}{\rho_0}$	$C_{ps,1}\frac{\mu}{\mu_0}$
P60	1.48	11.83	0.91	44.86	0.39	38.30
P120	1.48	5.91	1.25	19.31	0.53	13.29
P240	1.48	2.96	1.58	3.21	0.68	2.21

Table 3 Test samples for internal core

Notation	Hole diameter (mm)
H3	3
H4	4
H5	5
H6	6

20 Hz frequency. The following table shows the notations that will be followed for the internal core test samples for the current study (Table 3).

The internal core structure is investigated by varying the hole diameter on the cell walls. Change in the area of the hole affects the velocity which in turn changes the dynamic pressure of air for the same flow rate. The static pressure inside the cells can therefore be controlled by the variation of the area along the flow direction. To study the static pressure characteristics, 3D-printed core structures with different hole diameters were measured. Figure 12 shows core test specimen with internal cells that are separated by thin vertical walls. To measure the pressure drop characteristics, different test specimens were manufactured by varying the hole diameter.

A parameterized CAD-model was created with the software Catia V5R20 [24] to allow rapid geometry changes for the generation of test specimen variants. Four variants with increasing hole diameters from 3 to 6 mm are tested with dimensions shown in Fig. 12, (left). For the connection between the test specimen and the suction pipe of the flowbench, an adapter funnels were also designed (Fig. 11). All test specimens were printed using a Stereolithography(SLA)-printer Form 2, using the UV-light sensitive resin type Durable V2 or Clear provided by the manufacturer [25].

The SLA-prints revealed an unexpected poor accuracy of holes under 3 mm in diameter due to partial or full clogging, even though the chosen layer height of 0.01 mm should allow for more than accurate shapes of the holes in this scale. A pre-test is performed for studying the partial blockages of small holes within the SLA-printings. For this, a special test specimen was designed. Appendices 1 and 2 show the details of this pre-test and estimation of the effective diameter of the printed sample.

Figure 13 shows the measurement data of the pre-test. The diagram reveals good agreement between nominal (respectively, desired) and measured effective hole diameters for 3 mm and above. A partial hole blockage was observed for nominal hole diameters smaller than 1.5 mm, the tendency for partial blockage shows a hyperbolic trend with decreasing hole diameter: While the deviation is 5.3% for a diameter of 2 mm, it is already 12.1% for 1 mm and 46.3% for 0.47 mm holes up to throughout completely blocked holes (resp. 100%) from nominal diameters of 0.45 mm on and lower. The deviations between the nominal and measured effective diameters are taken into account in the evaluation of the measured internal pressure distribution as shown in Sect. 3.2.1.

3.2.1 Pressure characteristics of internal core structure

Test samples H3, H4, H5, and H6 were measured to compare the pressure characteristics of the single hole diameter with that of the analytical model shown in Eq. 16. The samples have a constant diameter along the flow direction. All samples measured have 11 holes normal to the flow direction. The pressure drop through hole is calculated as a function of velocity through the hole and compared with Goldstein analytical model. Cross section area was calculated depending on the number of holes normal to the flow to determine the velocity. Figure 14 shows the variation of the pressure drop measured using the static pressure taps.

From Fig. 14 for samples H3 to H6, the Goldstein model was able to predict the pressure drop close to the measurements for velocity up to 15 m/s. Above 15 m/s, the deviation from the analytical solution increases with an increase in velocity. The measured pressure drops are larger than the analytical model, which might be due to the jet effect at higher velocities.

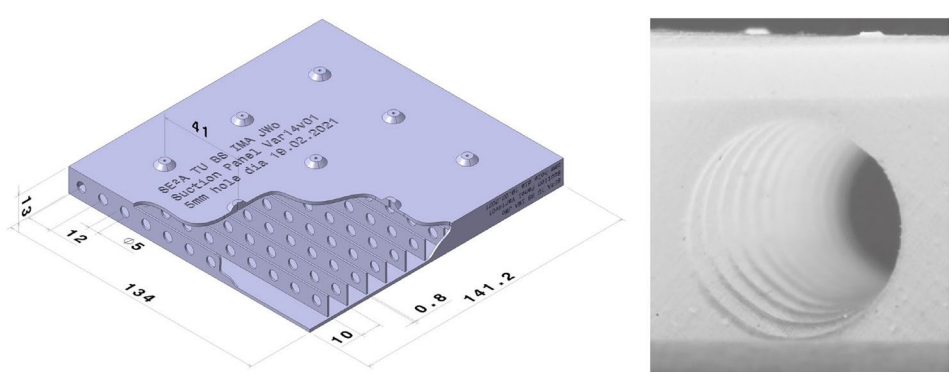

Fig. 12 CAD of the core test specimen (incl. sectioning) with 5 mm holes (left), Example of SLA hole quality (right)

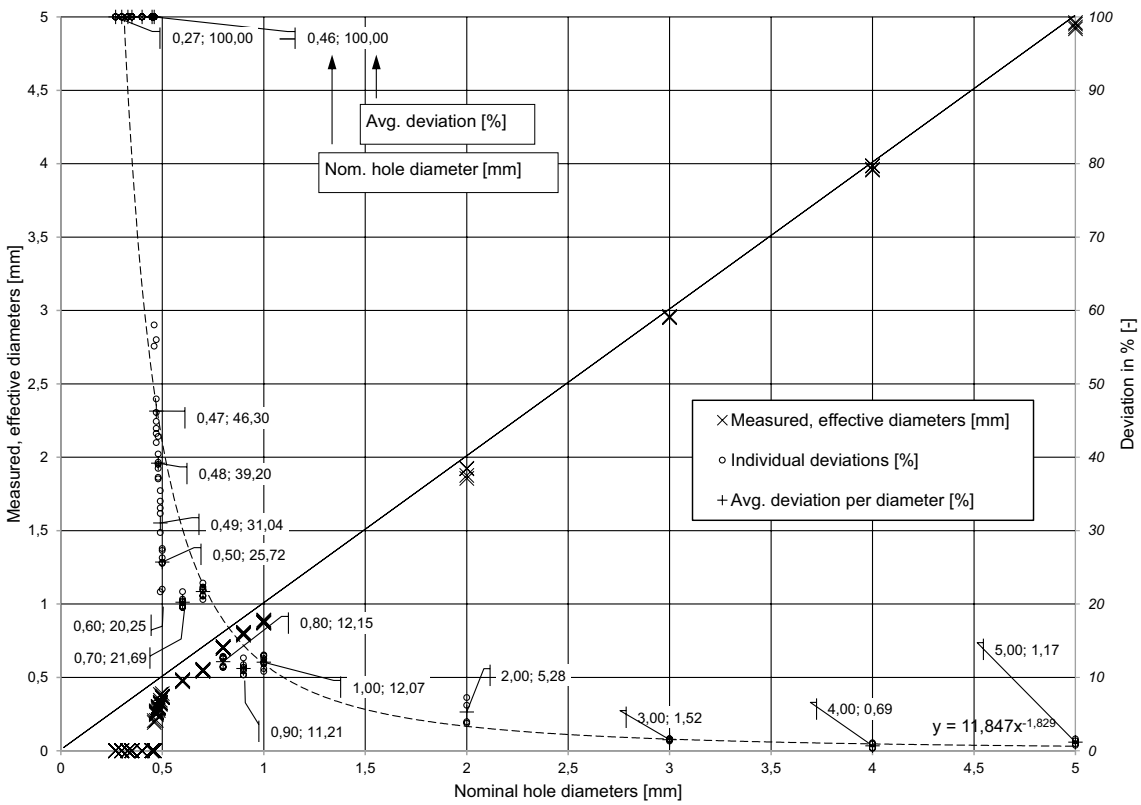

Fig. 13 Correlation between nominal (0.46–5 mm) and actual hole diameters, deviations in %

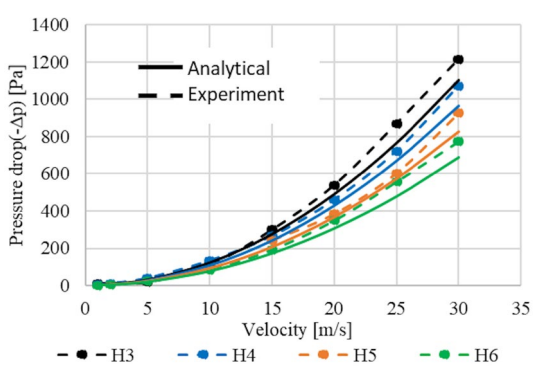

Fig. 14 Pressure drop through internal core with constant hole diameter

The 2 mm hole was not produced as a through hole and the effective cross section area is reduced due to print material residue (see Fig. 15). As seen in Fig. 13, the hole diameter of 2 mm showed a deviation of 5% to the nominal diameter. Based on the pretest on the 3D-printed, Fig. 13, it has been concluded that the 2 mm hole should be avoided for the internal core layout calculation. Therefore 3 mm is specified as the minimum possible diameter constraint in ASPeCT. Internal core's hole diameter variation is estimated based on the interpolated pressure characteristics (3–6 mm) as explained in Sect. 2.2 if the diameter and velocity are in this measurement range. It is also known that the 90° turn of the sucked air as it moves through the porous sheet and the internal core holes can affect the pressure characteristics. This effect is neglected based on the previous literature [13] on suction system design for sailplanes for the current study. The 90° turn of the sucked air is only expected to affect smaller diameters below 4 mm. Authors plan to verify this using measurements on 3D-printed internal core geometry combined with a porous sheet in the future.

Figure 16 shows the interpolated pressure drop characteristics for the hole diameter varying from 3 to 6 mm. Above this measurement range (say above 30 m/s), the coefficients based on the analytical model will be used by accounting for 10% deviation. By making this assumption, we are also making sure that the chamber design will provide at least the minimum requirement for maintaining the target suction needed for the xHLFC system.

4 Results and discussion: ASPeCT case studies

This section presents a case study of the suction system design for xHLFC subsonic airfoil. The airfoil is optimized for a Reynolds number of 16 Million and a cruise Mach

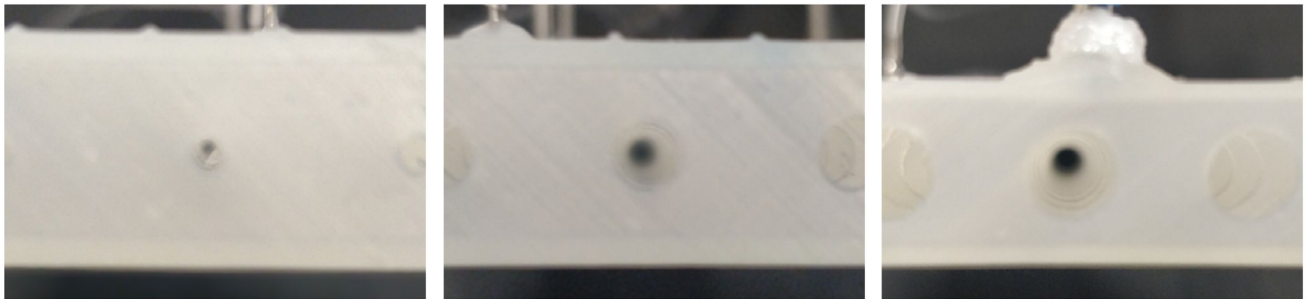

(a) H2 (b) H4 (c) H6

Fig. 15 Hole geometry comparison for 3D-printed samples

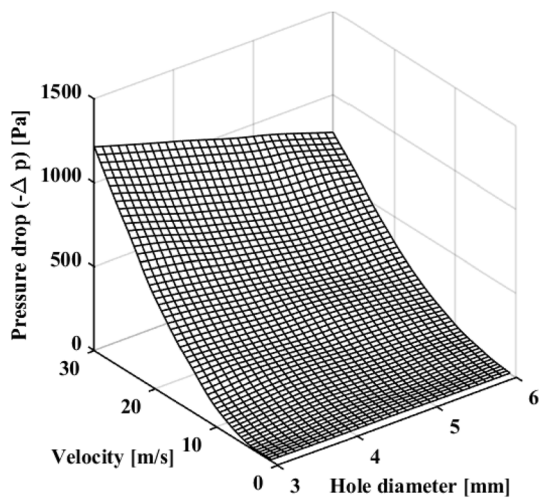

Fig. 16 Interpolated pressure characteristics

number of 0.4 for fully electric short-range aircraft [26, 27]. The shape of the airfoil and the suction velocity profile on the top surface was optimized using a genetic algorithm with an objective of 80% chordwise laminarisation [7]. The suction onset was constrained to be at least 50% chord. The maximum thickness of the airfoil is constrained to be more than 12% chord. The airfoil was optimized for a range of design C_l between 0.3 and 0.7. The flight mission profile and the initial design requirements of the airfoil are based on the overall aircraft design of the SE2A short range aircraft [28]. The optimized airfoil shape and optimized suction velocity profile used in the current study are shown in Fig. 17a, b respectively. The study analyzes the effect of a porous sheet, internal core, and lift coefficient on the suction power in three different subsections. The first part will deal with the impact of pressure characteristics of the porous sheet shown in Sect. 3.1.1 on the suction power. Secondly, the internal core design parameters are varied to study how the actual suction velocity and suction volume are affected by it. For this purpose, the study considers the internal core geometry

Table 4 Airfoil design conditions

Parameter	Value
Reynolds number	16 million
Mach number	0.4
Design C_l	0.4
Climb C_l	0.7
Flight altitude	8000 m
Start of suction	51%
End of suction	77%

and uses the pressure drop coefficients estimated as shown in Sect. 3.2.1 . Finally, ASPeCT analyzes the suction system performance with varying flight conditions and estimates the suction power for different lift coefficients ranging from 0.3 to 0.7. The current study focuses only on the suction system's aerodynamic requirements and neglects the structural requirement of stringers towards supporting the porous outer skin. Table 4 shows the design condition of the flight.

The suction velocity coefficient is multiplied by the flight velocity to determine the local suction velocity. The numerical tool then treats the velocity in each cell of the suction system as an average of the values at the endpoints of the cell. The suction volume flow rate is then estimated by accounting for the actual flow area based on the porosity and surface area blocked due to the internal core walls. This means that for the same volume flow, the actual velocity of flow through the porous sheet is higher for the perforated sheets with smaller holes.

4.1 Effect of pressure characteristics of porous sheet

This section discusses the effect of the perforated sheet on the suction power. To derive just the porous outer skin influence, we keep the internal core geometric parameters constant. Table 5 shows the porous sheet properties used in this study.

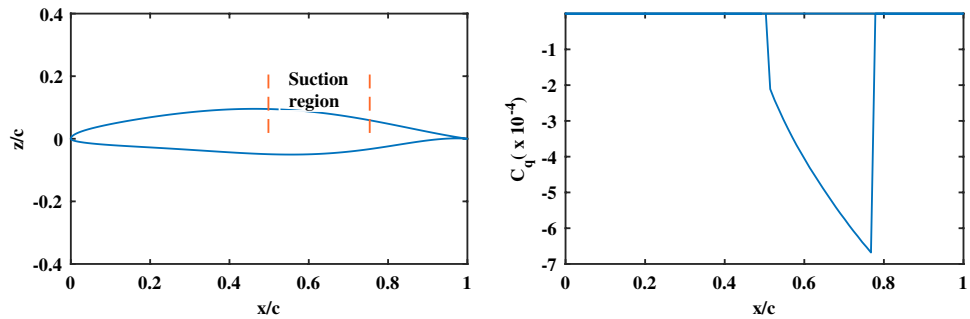

(a) Subsonic xHLFC airfoil (b) Target suction velocity coefficient

Fig. 17 Optimized airfoil shape and suction velocity coefficient

Table 5 Porous sheet properties

Parameter	Value
Porous sheet perforation (d_{ps})	60 µm, 120 µm, 240 µm,
Porosity	0.9 %
Hole spacing	$10 \times d_{ps}$

For the calculation of the pressure and velocity variation on the top surface of the airfoil, XFOILSUC simulations are used. The approach used here takes into account the lowest C_l (0.3) in the design range. The effect of changing lift coefficient to the suction power is discussed in detail in Sect. 4.3.

ASPeCT is allowed to freely calculate the cell wall hole diameter thereby making sure that in each cell the target suction velocity is attained. Figure 18b shows the pressure drop through the porous sheet for each cell in the suction region.

As expected, based on the pressure measurement of the perforated sheets, Fig. 18b shows a higher pressure drop for the 60 µm case. The pressure drop is approximately four times that of the largest diameter of 240 µm. The pressure drop characteristics do not single-handedly decide to choose the micro-perforated skin for the xHLFC suction system.

Figure 19 shows the solid line which is the boundary between laminar and turbulent flow as measured by Pfenninger [29, Page 3–35 Fig. 5]. On the left side of the line, the flow is expected to be laminar owing to either low suction flow rate or higher hole pitch. As a certain minimum amount of suction flow rate is required to keep the flow laminar therefore interplay between hole pitch and hole diameter determine the laminar-turbulent transition. For perforated plates with lower hole pitch, there is a possibilty of hole vortices interaction that can create instability and make the flow turbulent. Study from Macmanus and Eaton [11] suggest that hole pitch above 15 times the diameter can also cause vortices interaction for HLFC application with boundary layer thickness in the order of 200 µm. From Fig. 19 we can expect all three perforated sheets considered to develop decaying hole vortices for the suction flow rate considered. It is important to note here that as the perforation's diameter increases, the curve shifts right. Based on this observation, the higher the perforation's diameter, the greater the chance to add suction-generated instabilities into the flow.

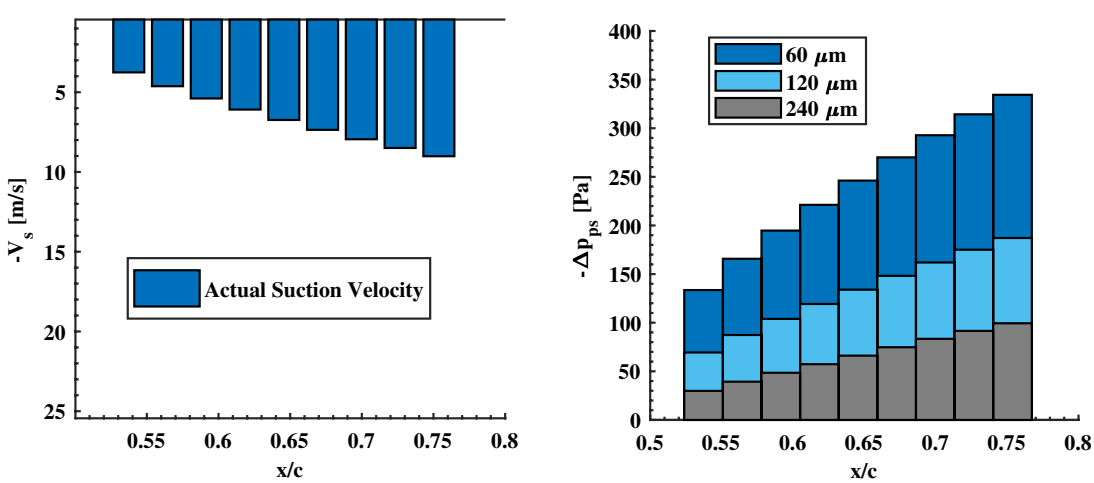

(a) Average suction velocity through porous sheet in each cell (b) Pressure drop for different porous sheet perforation

Fig. 18 Comparison of pressure drop through porous sheet for same suction velocity

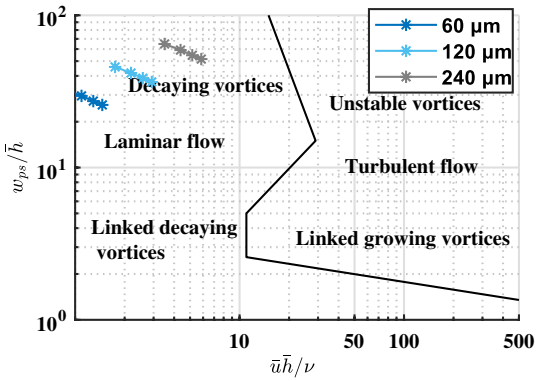

Fig. 19 Pfenninger criterion check for the different perforation (adapted from [29])

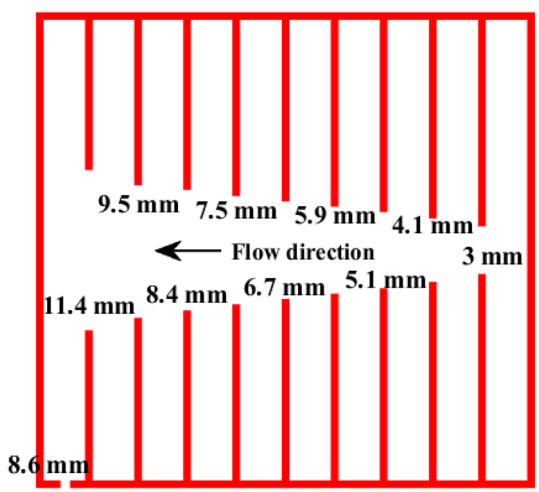

Fig. 20 Schematic of optimized internal core layout computed for $d_{ps} = 240\,\mu m$ and $C_1 = 0.3$

More detailed numerical analysis is needed in this regard and is out of the scope of this paper. Based on Fig. 19, the 240 micrometre perforation with a hole spacing of 10 times the diameter does not negatively affect the laminarity of the outer flow for the suction flow rates considered however may lead to instabilities at higher flow rates.

Two design approaches are possible for the internal core design. In the first approach for each design point, different layout of the internal core can be computed. The second approach computes the internal core layout based on single design point and then vary the suction power to handle the rest. The second approach is demonstrated here as the same internal core layout, shown in Fig. 20, is used to work with three different perforated metallic. The throttle hole diameter depends on the difference between the static pressure in the cell and the plenum pressure. For the current study, the throttle hole diameter is calculated for a fixed pressure difference to the plenum.To make sure

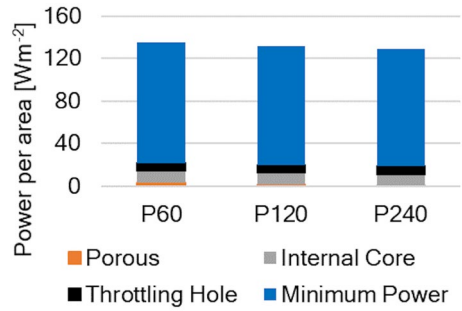

Fig. 21 Comparison of suction power for different porous sheets

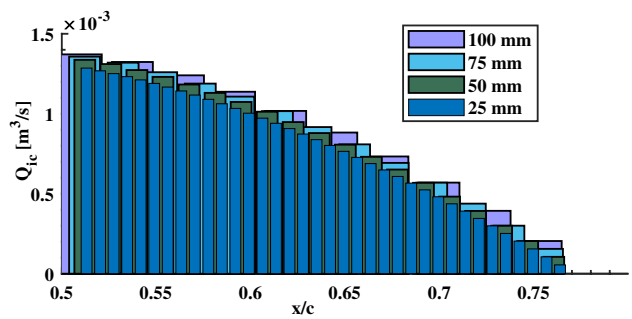

Fig. 22 Variation of volume flow rate inside internal core for different cell width

that the throttle hole diameter is below 10 mm the pressure difference to plenum is considered to be 500 Pa.

Figure 21 shows the influence of hole diameter of the metallic outer sheet on the total suction power. As expected, the 60 µm sample has the highest suction power requirement due to a smaller perforation diameter. The increase in power to suck through the 60 µm porous sheet increases approximately four times that of the 240 µm sheet, which is also in line with the pressure drop characteristics shown in Fig 18b. However, the total suction power does not show a significant increase as the porous sheet only accounts for less than 5% of the total suction power.

4.2 Effect of internal core parameters

ASPeCT investigates the variation of the internal core cell width for constant cell wall thickness of 2 mm and constant span-wise hole spacing of 25 mm. The cell width is varied from 25 to 100 mm with a step of 25 mm. Based on the cell width, spanwise hole spacing and the suction velocity, the volume flow rate in the internal core layout is computed for $C_1 = 0.3$ considering a porous sheet of perforation of 120 µm. ASPeCT studies the effect of the internal core parameters on the hole layout and the suction power of the xHLFC system.

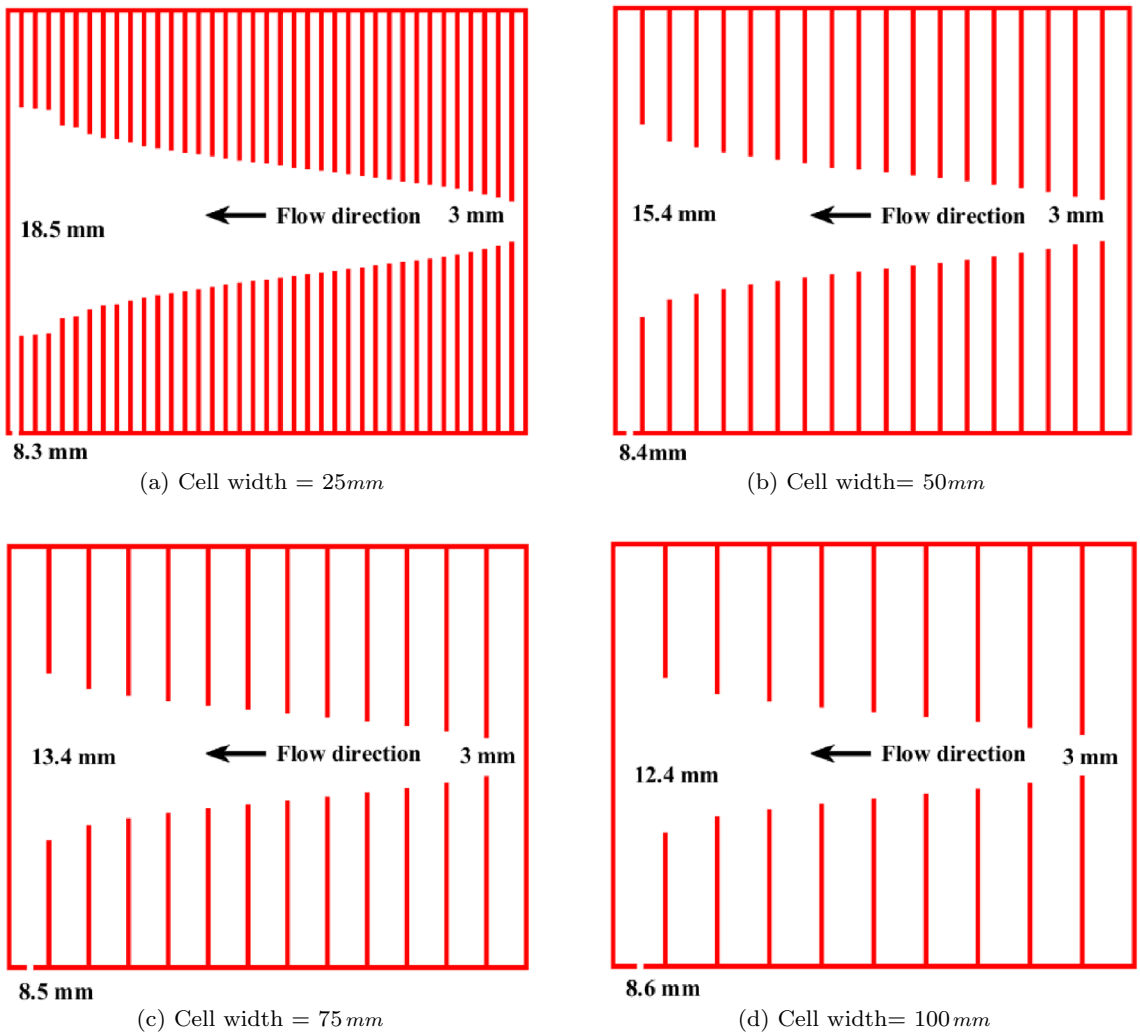

Fig. 23 Comparison of internal core layout schematic (C_l = 0.3 and d_{ps} = 120μm)

The airfoil has a suction region length of 26% chord. Increasing cell width means the number of cells in the suction region decreases. As the number of cells decreases, the volume flow rate inside the cell increases to keep the total suction volume constant. Figure 22 shows the comparison of volume flow rate per cell with varying cell width.

With the help of the pressure characteristics obtained from the flowbench measurements (Sect. 4.2), the code ASPeCT calculates an optimized hole diameter for each of these cell width considered. The optimized internal core provides the necessary pressure difference to achieve the required suction profile for the airfoil. Figure 23 shows the different optimized layout for these cases.

Figure 23 shows the effect of cell width on the internal core layout. The calculation for the first cell starts at the end point of the suction region (77%). The volume (Q_{ic}) in each cell (except the first cell) is a combination of suction through through the porous sheet as well the air flow from the adjacent cell to the right of it. The visible difference at the start of suction is because of the numerical discretisation of the cell width values. This can be adjusted by manually modifying the target suction velocity profile input. The internal core layouts differ in maximum hole diameter calculated on the cell wall. The layout shows only the maximum and minimum diameter for better readability. For smaller cell width of 25 mm (Fig. 23a), the maximum diameter is 18.5 mm. All computed layouts can provide enough pressure drop along the chordwise direction to enable suction from the airfoil's adverse pressure region. An increase in the cell by four times reduces the maximum hole diameter by 40%. This reduction is mainly because of the increased flow rate in each cell, producing the required pressure drop with a lower diameter. The maximum hole diameter in the core influences the total height of the suction system. The volume flow rate inside the cell varies with the cell width, and even though

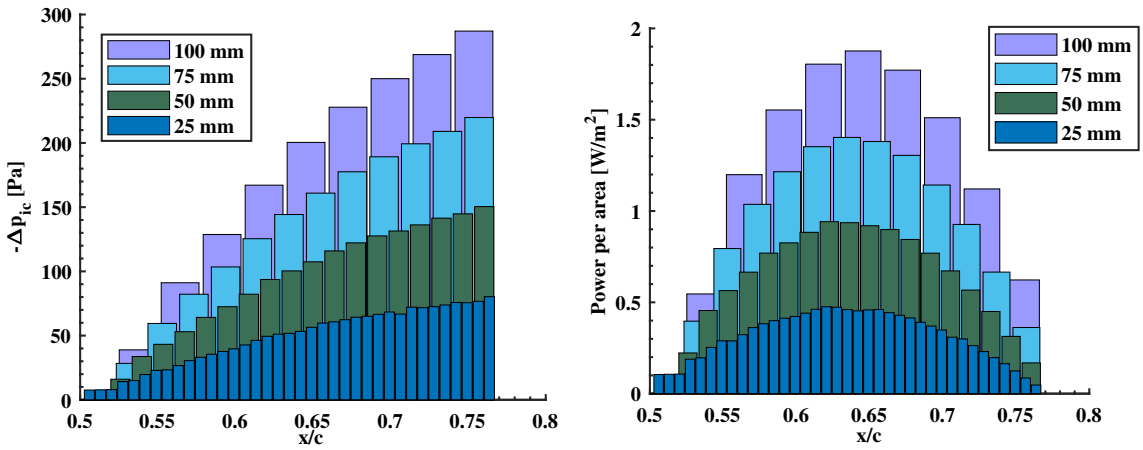

(a) Pressure drop in internal core cell wall

(b) Required power inside internal core

Fig. 24 Pressure and required power inside internal core as a function of cell width

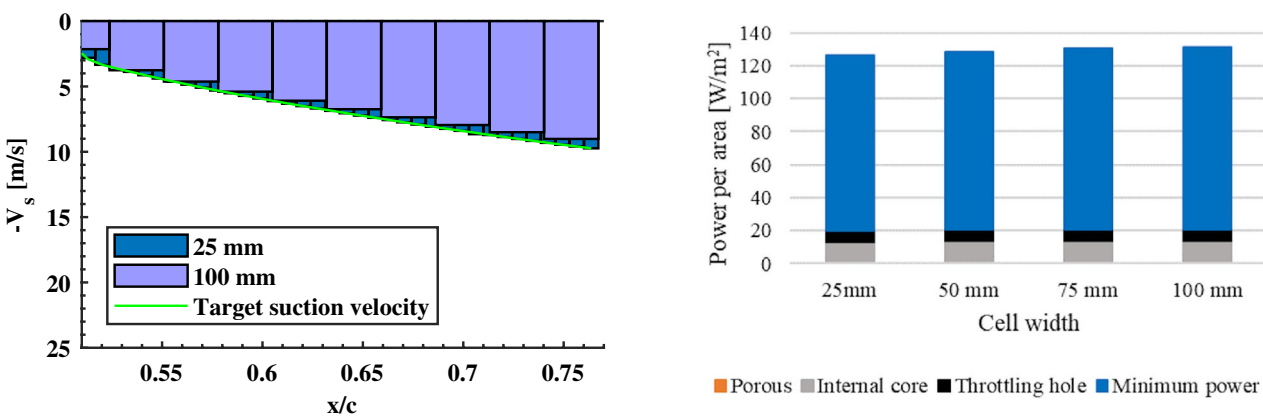

(a) Suction velocity comparison for cell width 25mm and 100 mm

(b) Total suction power comparison

Fig. 25 Effect of internal core cell width on suction velocity and power

the power to suck the air through each cell wall changes, the cumulative power of the buffer practically remains the same for the same suction velocity profile considered. Figure 24 shows the pressure and power breakup for each cell of the internal core.

But it should also be noted that as the cell width increases, the suction profile will be more discrete in nature. This is because the suction velocity in each cell is assumed to be an average of the optimum suction velocity calculated at the end points of the cell. As the cell width reduces, the calculated suction velocity closely follows the target suction velocity profile. The discrete nature of the suction velocity can be seen in Fig. 25a. Cell width of 25 mm captures the target suction profile quite well compared to the larger cell width of 100 mm. Therefore the choice of cell width should be a compromise between the space available for integration of suction system and how accurately the target suction velocity needs to be captured.

Figure 25a compares the suction power required for different cell widths. The total suction power does not significantly vary with cell width since all the cases drive the same target suction velocity. The power in the first cell which is near the trailing edge is influenced by the volume flow rate through the porous sheet and the pressure difference occurring as the air moves to the next cell. In the next cells volume flow contribution comes from both through the porous sheet as well as from the upstream cell . This increases the power contribution per cell as we move towards the start of the suction region. The major factor to the power is the energy to drive the sucked air back to atmospheric condition. For the different cell widths considered, the static pressure at the cell above the throttle hole has to be the same to ensure the suction

velocity matches the target suction velocity. Based on the ideal power calculation, the total volume of sucked air is pushed back to the atmosphere at flight velocity at a similar expense of power for different cell width considered. The internal core layout with the cell width of 25 mm shows approximately 2% less power than the 100 mm case, mainly owing to a slightly higher volume flow rate inside the internal core cell, which accounts in the internal core contribution. Comparing the power values in Fig. 25b we can see that the total contribution of porous sheet, internal core and throttle hole accounts for approximately 20% of the ideal power calculated.

4.3 Effect of changing flight conditions

The previous sections discussed the designed suction system layout performance at the single lift coefficient of 0.3, which is the smallest in the range of lift coefficients of the airfoil. As a further check, it is essential to see the suction system and internal core layout designed for the lift coefficient of 0.3 perform at different flight conditions. The cell layout optimized with pressure characteristics of the 60 µm metallic sheet as shown in Fig. 26 is used for this study.

The suction profile shown in Fig. 17b can perform in a range of lift coefficients from 0.3 to 0.7. This is because the optimizer accounted for this range of lift coefficients while calculating the suction profile. So if the freestream velocity remains constant, the same suction velocity coefficient can be used at lift coefficients from 0.3 to 0.7. Figure 27 shows C_p variation for the range of lift coefficients for the airfoil.

As lift coefficient is increased, the suction system works from a lower pressure over the airfoil surface as seen in Fig. 27. Figure 28 shows an example of what happens inside the cells if the suction power is kept the same with value calculated at a lift coefficient of $C_l = 0.3$. The pressure on the airfoil surface near the first few cells (near 75% of chord) is similar for the range of lift coefficients, therefore, enabling

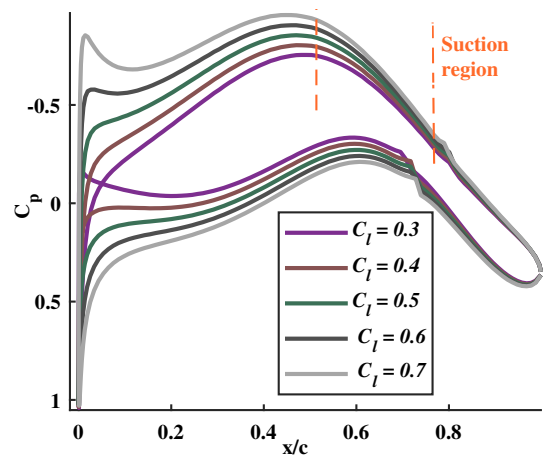

Fig. 27 Pressure variation on airfoil with C_l

suction through the porous sheet. However, the target suction velocity cannot be achieved in the remaining cells (from 60 to 50% of the chord). To ensure that the boundary layer suction remains active even at off-design conditions, we have to adjust the suction pressure developed inside the internal core to the new static pressure on the airfoil.

Figure 29 shows that by increasing the suction power the minimum suction velocity requirement is also achieved for higher lift coefficients. The suction volume flow rate was gradually increased until the suction velocity in the cell matches the target suction velocity required. This was made possible by using a multiplying factor to scale up the volume flow rate into each cell.

The multiplying factor was then manually adjusted till velocity inside the cell reaches the target suction velocity. A typical mission profile for the short range aircraft shows that the flight will be in cruise at lift coefficient of 0.4, while

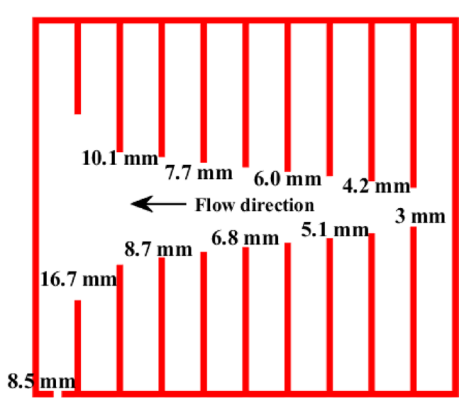

Fig. 26 Schematic of optimized core layout for $C_l = 0.3$, $d_{ps} = 60$ µm and cell width = 100 mm

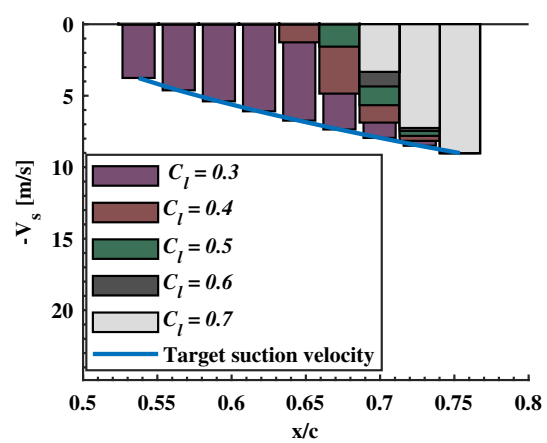

Fig. 28 Example showing suction at different C_l for same pressure below the porous sheet as $C_l = 0.3$

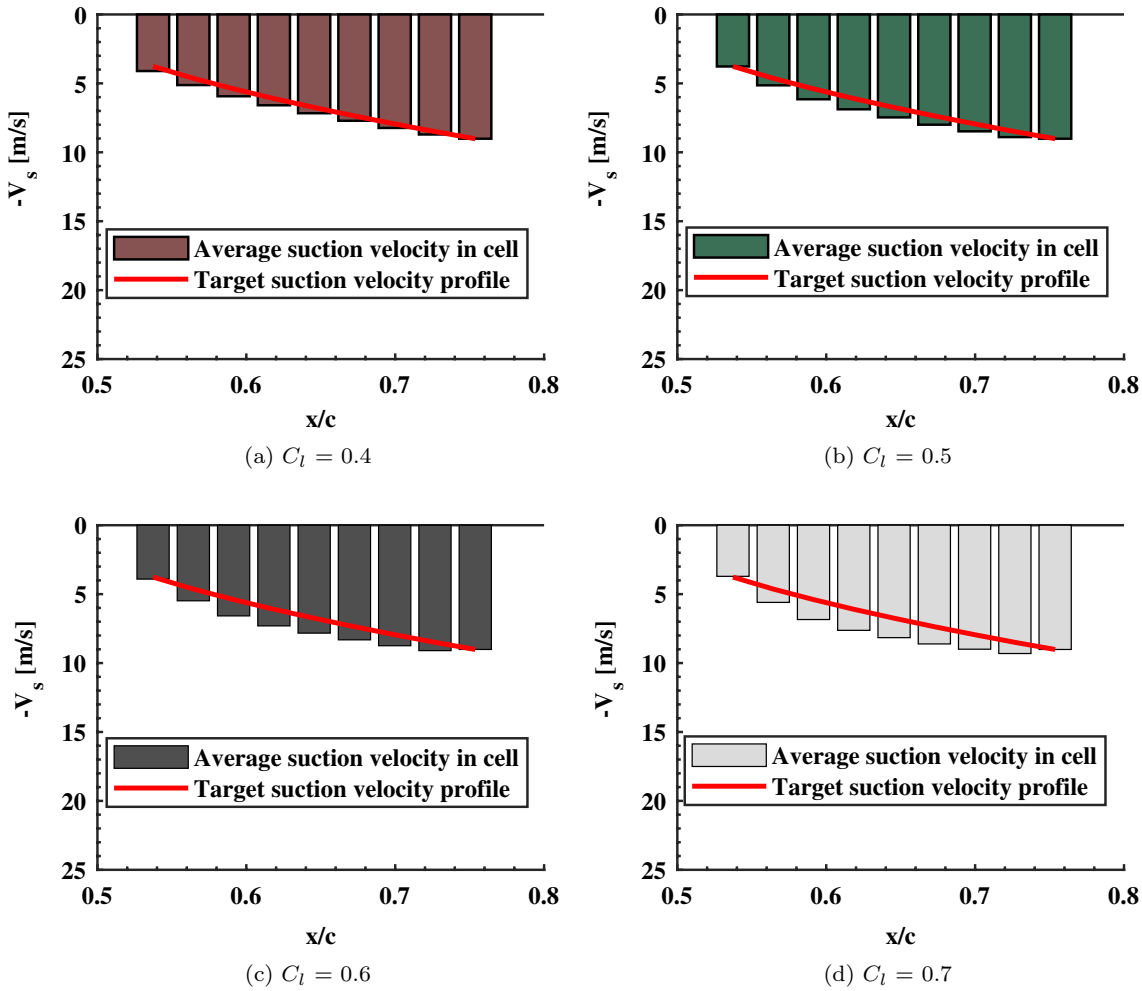

Fig. 29 Suction velocity comparison for different lift coefficient with increased suction rate

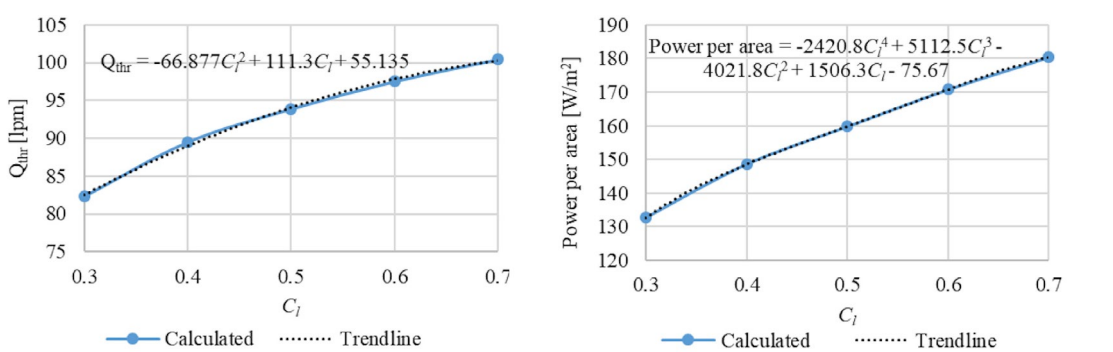

(a) Variation of volume flow rate with lift coefficient (b) Variation of suction power per buffer with lift coefficient

Fig. 30 Effect of lift coefficient on suction volume and power

the off-design conditions will be at a higher lift coefficient in the range of 0.6–0.7 for climb. Based on the calculations performed, the internal core layout will be able to perform well in this range of lift coefficients. The suction volume flow rate per throttle hole required to maintain the optimum suction is then compared for each lift coefficient. Figure 30a shows the suction requirement as a function of lift coefficient based on this study.

From Fig. 30a it can be inferred that the suction requirement increases as a non-linear function of lift coefficient. The calculated volume flow requirement is closely fitted with help of a quadratic curve trend line. The variation of suction volume means that the power required to maintain this suction will vary with two order higher magnitude. This is because suction power is a product of volume flow rate and pressure loss. The variation in power per throttle hole as a function of lift coefficient is shown in Fig. 30b.

Finally, the airfoil polar for the actual and target suction velocity coefficient is compared in Fig. 31. The polars are calculated using XFOILSUC [17] for C_l in the range of 0.3–0.7 with a step of 0.1. The total drag based on the actual suction profile closely follows that of the target suction profile calculation.This is expected because the internal core is optimized targeting the optimum suction profile which also accounts for the ideal suction power. Even though the actual suction volume is slightly higher compared to the target suction velocity at a higher C_l, this does not contribute to further drag reduction. The slight increase in the total drag compared to the calculation with the target suction velocity profile is due to the suction drag contribution (Fig. 25) from the porous sheet and the internal core.

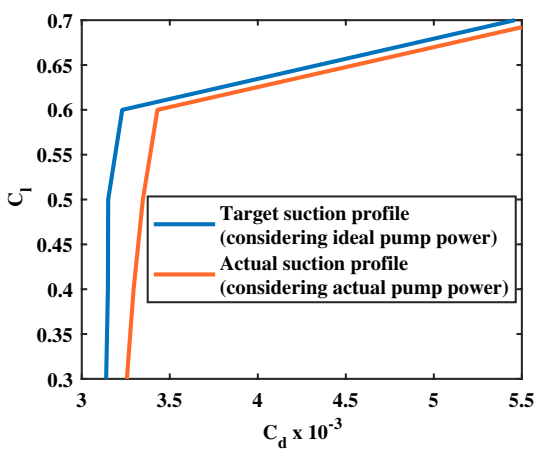

Fig. 31 Comparison of total drag based on target and actual suction velocity profile

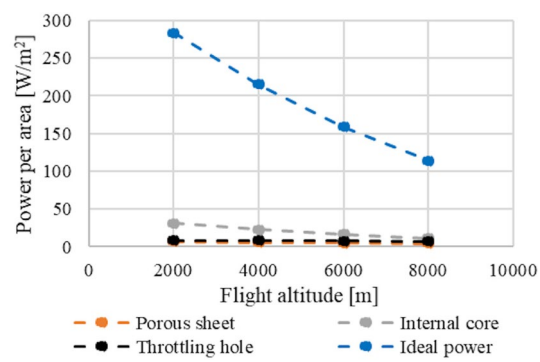

Fig. 33 Power breakdown for the xHLFC suction system with flight altitude

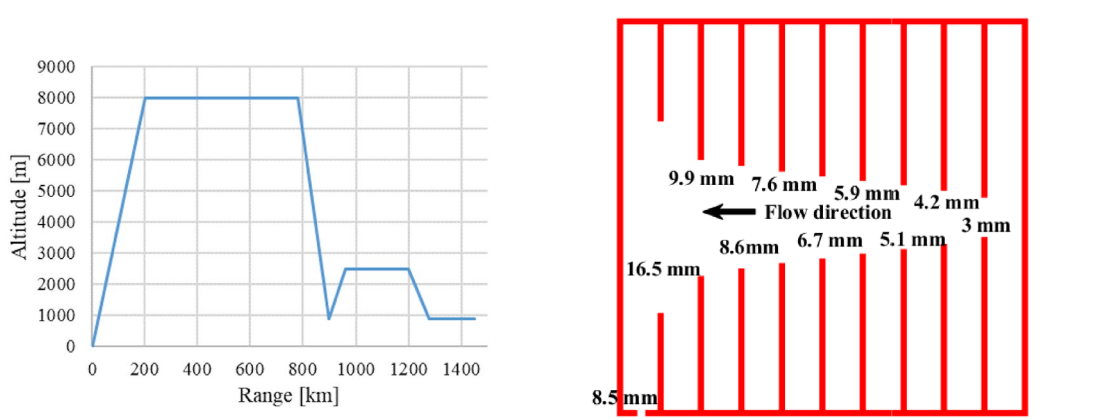

(a) SE2A short-range flight mission profile (b) Internal core designed for cruise condition for $d_{ps} = 60\mu m$

Fig. 32 Mission profile and internal core layout designed for cruise conditions

4.4 Variation of power contribution from porous sheet with flight altitude

An additional study was performed to investigate how the flight altitude influences the suction power of the xHLFC system. The suction system layout was initially computed for the design C_l of 0.4 and cruise Mach number of 0.4 at an altitude 8000 m. Figure 32 shows the mission profile and the internal core layout used for this study.

Based on the mission profile [28] the reserve cruise altitude is 2500 m. Therefore, an analysis was performed for different altitudes between 2000 and 8000 m with an interval of 2000 *m* to maintain the same target suction velocity profile (Fig. 17b). Figure 33 shows the variation of the power per unit area for the xHLFC suction system at different flight altitudes.

Figure 33 shows that the calculated power decreases linearly with flight altitude. As the altitude increases, the density and the pressure around the airfoil reduces. This decreases the suction power requirement of the pump ,i.e, less power is needed at 8000 m compared to 2000 m. The pressure loss through the porous sheet (orange line) also varies linearly as the porosity coefficients scale with the air properties (Table 2). More detailed analysis is required to treat the off-design conditions combining the effect of altitude, lift coefficient and flight velocity. This is planned in future work where the design tool ASPeCT will be extended for the transonic aircraft.

5 Conclusion

The MATLAB design tool ASPeCT developed for the substructure design for the short-range airfoil accounts for the pressure properties of the porous sheet and the internal core. The design of the suction system for the xHLFC system starts with the porous outer skin. The pressure drop through the perforated metallic sheet was measured at mean sea level conditions and was then scaled to the flight altitude to account for the variation in density and viscosity. The pressure drop characteristic of the porous sheet shows a quadratic trend and as expected, the perforated sheet with a smaller perforation diameter has larger pressure drop. ASPeCT was formulated to incorporate this change in pressure characteristics in the calculation of total suction power. Since the suction system for the xHLFC system works under the airfoil's adverse pressure region, it is necessary to consider the additional pressure drop due to suction from the boundary layer. The study accounted for this using the modified semi-empirical Bohning–Doerffer model. Numerical calculations regarding the inter-hole vortice interaction were considered in the code and compared with modified Pfenninger criterion based on the suction volume per hole on the porous sheet. Direct numerical simulations are needed in this regard to further understand the interplay of hole-generated vortices in the laminar flow behaviour over the porous surface.

The flowbench measurements on the 3D-printed internal core structures established the pressure drop as a function of the diameter of the hole and velocity. The measured results were in good agreement with the analytical Goldstein model for low flow rates and hole diameter above 2 mm. The numerical study of the sensitivity of the suction velocity to the internal structure's cell width showcased that increasing cell width affects the target suction velocity discretization. The final decision on the cell width should be a compromise between the wing's manufacturing and space constraints and the accuracy with which the target suction profile needs to be captured.

The suction power of the designed system was calculated by assuming unit efficiency for the systems involved and neglecting duct losses. The contribution of the porous sheet, internal core, and throttling hole accounts for approximately 20% of the ideal power. The ability of an internal core layout in performing at varying flight conditions was discussed. The study established the suction volume requirement of the system at these conditions. The suction volume flow varies as a quadratic function of the lift coefficient. The trend line obtained can be used to understand exactly how much power is needed for the boundary layer suction system to remain active at a given lift coefficient.

With the decrease in the flight altitude, the total suction increased linearly for maintaining the same suction flow rate as the cruise altitude. The suction power requirement is lower at higher altitude owing to the lower density of the air. The scaling of the porosity coefficients also played a role in the power contribution from the porous sheet. However, detailed investigations are planned in the near future to take into account the exact suction requirement and flight velocity based on the overall aircraft design.

Appendix 1: 3D-printed pre-test specimens

See Table 6.

Table 6 Specification of 3D-printed hole pre-test specimens, nominal hole diameters and results

Specimen no.	No. of holes	Nominal hole diameter (mm)	Actual effective hole diameter (mm)	Avg. deviation (%)	Std. deviation (mm)
PNo78	4	5	4.9414	1.17	0.0194
PNo78	4	4	3.9725	0.69	0.0152
PNo78	4	3	2.9545	1.52	0.0042
PNo78	4	2	1.8944	5.28	0.0342
PNo5	7	1	0.8793	12.07	0.0085
PNo15	7	0.9	0.7991	11.21	0.0073
PNo5	7	0.8	0.7028	12.15	0.0054
PNo14	7	0.7	0.5481	21.69	0.0055
PNo15	7	0.6	0.4785	20.25	0.0046
PNo5	6	0.5	0.3714	25.72	0.0999
PNo20	6	0.49	0.3379	31.04	0.0244
PNo20	7	0.48	0.2918	39.2	0.0095
PNo20	7	0.47	0.2524	46.3	0.0239
PNo20	7	0.46	0.0571	100	N/A
PNo14	7	0.45	0	100	N/A
PNo15	7	0.4	0	100	N/A
PNo15	7	0.35	0	100	N/A
PNo14	7	0.33	0	100	N/A
PNo5	7	0.3	0	100	N/A
PNo14	7	0.27	0	100	N/A

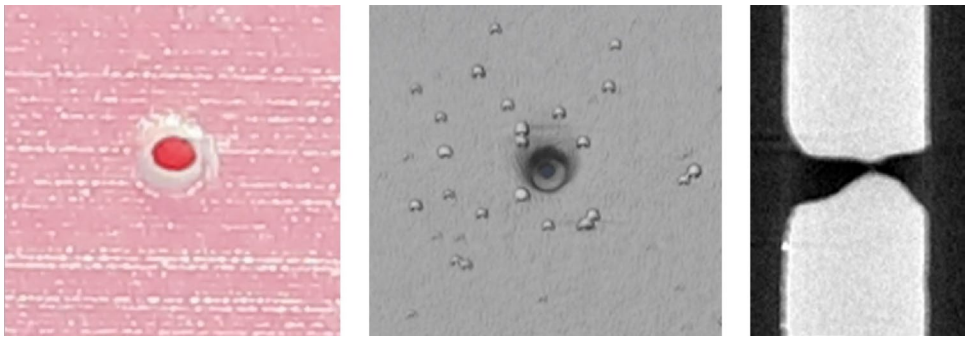

Fig. 34 Partially blocked hole in SLA-printed test specimen with CT-scan

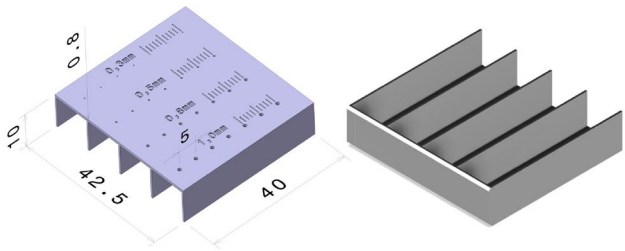

Fig. 35 CAD-model of a hole test specimen with four rows of seven holes with diameters of 0.3, 0.5, 0.8 and 1 mm

Appendix 2: Evaluation of small circular hole accuracy in SLA-printed parts

Figure 34 shows the high resolution pictures as well as a CT-Scan of the printed holes. Partial or full clogging of the holes is observed due to the capillary effect causing excess liquid resin to rest in the holes.

Figure 35 shows the pre-test test specimen to study the hole accuracy of the printed parts. These pre-test specimens represent the actual test specimens geometrically in terms of wall thicknesses, printing settings, used printer and resin

Fig. 36 Camera setup for optical analysis of test specimen (left). Measured, effective diameters (blue font) for nominal diameter (0.3, 0.5, 0.8 and 1 mm) (right)

type. The specimens offer varying hole diameters from 0.27 to 5 mm according to Table 6 in Appendix 1.

The pre-test specimen is then subjected to optical analysis to study the holes in the face sheets. The face sheet surfaces were photographed at high resolution (30.4 megapixel resolution, resulting in images with 6720 × 4480 pixels) using an SLR-camera Canon EOS 5D Mark IV. The camera is fitted Carl Zeiss Milvus 2/100M macro lens due to its high planarity and minimal distortion shown in Fig. 36, left. Brightness and pixel contrast between surface and background were maximized with the help of Digital Photo Professional 4 software [30]. Contour sizes as well as hole areas are computed with a Python 3 routine [31] on pixel basis. The holes are detected based on the color contrast at the boundary. Effective hole diameters and open areas are derived by averaging all dark pixels per hole. For this, the hole test specimens got printed with regular, linear indentations next to the holes, Fig. 35, left and Fig. 36, right. The indentations are used as scale and, combined with the resolution of the picture to estimate the area covered by each pixel. The amount of (dark) pixels per hole indicates the total opening area of each hole. The chosen resolution (say over 100 pixels within the smallest holes of 0.3 mm diameter) minimizes the tessellation effect. From the resulting hole area, the diameter of a representative, circular hole with same opening area is derived and is termed as the measured, effective diameter in Fig. 13

Acknowledgements We would like to acknowledge the funding by the Deutsche Forschungsgemeinschaft (DFG, German Research Foundation) under Germany's Excellence Strategy-EXC 2163/1-Sustainable and Energy Efficient Aviation-Project-ID 390881007. We would also like to acknowledge Dr. Arne Seitz (Research Engineer, Institute of Aerodynamics and Flow Technology, DLR, Braunschweig) for his guidance in porous sheet measurements using the Large Flowmeter test facility at DLR.

Funding Open Access funding enabled and organized by Projekt DEAL.

Open Access This article is licensed under a Creative Commons Attribution 4.0 International License, which permits use, sharing, adaptation, distribution and reproduction in any medium or format, as long as you give appropriate credit to the original author(s) and the source, provide a link to the Creative Commons licence, and indicate if changes were made. The images or other third party material in this article are included in the article's Creative Commons licence, unless indicated otherwise in a credit line to the material. If material is not included in the article's Creative Commons licence and your intended use is not permitted by statutory regulation or exceeds the permitted use, you will need to obtain permission directly from the copyright holder. To view a copy of this licence, visit http://creativecommons.org/licenses/by/4.0/.

References

1. Schrauf, G.: Status and perspectives of laminar flow. Aeronaut. J. **109**(1102), 639–644 (2005). https://doi.org/10.1017/S000192400000097X
2. Somers, D.M.: Subsonic Natural-Laminar-Flow Airfoils. Springer, New York (1992). https://doi.org/10.1007/978-1-4612-2872-1_4
3. Schrauf, G., Frhr. von Geyr, H.: Simplified hybrid laminar flow control for transport aircraft. In: ECCOMAS 2012—European Congress on Computational Methods in Applied Sciences and Engineering, pp. 3831–3842 (2012)
4. Joslin, R.: Overview of laminar flow control. NASA technical paper. NASA (1998). https://books.google.de/books?id=UgcVAQAAIAAJ
5. Beck, N., Landa, T., Seitz, A., Boermans, L., Liu, Y., Radespiel, R.: Drag reduction by laminar flow control. energies **11**(1) (2018). https://doi.org/10.3390/en11010252. https://www.mdpi.com/1996-1073/11/1/252
6. Horn, M., Seitz, A., Schneider, M.: Cost-effective HLFC design concept for transport aircraft. Deutscher Luft- und Raumfahrtkongress 2019 (2019)
7. Sudhi, A., Elham, A., Badrya, C.: Coupled boundary layer suction and airfoil shape optimization for HLFC application. AIAA J. (2020). https://doi.org/10.2514/1.J060480
8. Srinivasan, K.: Bertram: preliminary design and system considerations for an active hybrid laminar flow control system. Aerospace **6**(10), 109 (2019). https://doi.org/10.3390/aerospace6100109

9. Doerffer, P.P., Bohning, R.: Modelling of perforated plate aerodynamics performance. Aerosp. Sci. Technol. **4**(8), 525–534 (2000). https://doi.org/10.1016/S1270-9638(00)01063-4
10. Prasannakumar, A., Corelli, M., Seitz, A., Badrya, C.: Transpiration pressure loss and suction threshold on a flat-plate employing boundary layer suction. AIAA SCITECH-2021 Forum (2021). https://doi.org/10.2514/6.2021-1215
11. MacManus, D.G., Eaton, J.A.: Measurement and analysis of the flowfields induced by suction perforations. AIAA J. **36**(9), 1553–1561 (1998). https://doi.org/10.2514/2.563
12. Goldstein, S.: Modern Developments in Fluid Dynamics: An Account of Theory and Experiment Relating to Boundary Layers, Turbulent Motion and Wakes, vol. 1, pp. 299–308. Clarendon Press, Oxford (1938)
13. Bronkhorst, A.J.: Pressure Loss Measurements and Structural Analysis for the Production of a Sailplane Wing Section with Boundary Layer Suction. Master's thesis, TU Delft (2008)
14. Drela, M.: XFOIL: An Analysis and Design System for Low Reynolds Number Airfoils, vol. 54. Springer, Berlin (1989). https://doi.org/10.1007/978-3-642-84010-41
15. Ferreira, C.: Implementation of Boundary Layer Suction in XFOIL and Application of Suction Powered by Solar Cells at High Performance Sailplanes. Master's thesis, TU Delft (2002)
16. Broers, R.: Extending XFOIL and xSoaring for Suction-Type Boundary Layer Control Calculations. Master's thesis, TU Delft (2004)
17. Bongers, J.: Implementation of a New Transition Prediction Method in XFOIL. Master's thesis, TU Delft (2006)
18. Atkin, C.: Performance trade-off studies for a retrofit hybrid laminar flow control. System (2004). https://doi.org/10.2514/6.2004-2215
19. Saeed, T.I., Graham, W.R., Hall, C.A.: Boundary-layer suction system design for laminar-flying-wing aircraft. J. Aircr. **48**(4), 1368–1379 (2011). https://doi.org/10.2514/1.C031283
20. Pankhurst, R.C.: Power Requirements for Distributed Suction—For Increasing Maximum Lift. Aeronautical Research Council Tech. Rept. C.P. No. 82, p. 12 (1952)
21. Schlichting, H., Gersten, K.: Boundary-Layer Theory, 9th edn. Springer, Berlin (2017). https://doi.org/10.1007/978-3-662-52919-5
22. Preist, J., Paluch, B.: Design Specification and Inspection of Perforated Panels for HLFC Suction Systems. European Forum on Laminar Flow Control, Bordeaux (1996)
23. Seitz, A.: Messkörper, Durchflussmesssystem und Computerprogramm dafür. Patent DE102015113999 (2016)
24. Dassault Systémes: (2021). https://www.3ds.com/products-services/catia/products/
25. Formlabs Inc.: (2021). https://formlabs.com
26. Horst, P., Elham, A., Radespiel, R.: Reduction of Aircraft Drag, Loads and Mass for Energy Transition in Aeronautics. Deutsche Gesellschaft für Luft- und Raumfahrt- Lilienthal-Oberth e.V.. (Text). (2021). https://doi.org/10.25967/530164
27. Valerio, M., Karpuk, S., Sudhi, A., Badrya, C., Elham, A.: Multidisciplinary design optimization of a fully electric regional aircraft wing with active flow control technology. Aeronaut. J. under peer review (2021)
28. Karpuk, S., Elham, A.: Influence of novel airframe technologies on the feasibility of fully-electric regional aviation. Aerospace (2021). https://doi.org/10.3390/aerospace8060163. https://www.mdpi.com/2226-4310/8/6/163
29. Pfenninger, W.: Laminar Flow Control, Laminarization. AGARD Report No: 654 Special course on concepts of drag reduction p. 3 (1977)
30. Canon: Canon Deutschland GmbH (2021). https://www.canon.de/support/consumer_products/software/digital-photo-professional.html?os=windows%2010%20(64-bit) &language=
31. Python Software Foundation: (2021). https://devguide.python.org/

Publisher's Note Springer Nature remains neutral with regard to jurisdictional claims in published mapsand institutional affiliations.